Biosensors and Bioelectronics 141 (2019) 111384

Contents lists available at ScienceDirect

Biosensors and Bioelectronics

journal homepage: www.elsevier.com/locate/bios

Graphene-based nano composites and their applications. A review

Abdulazeez T. Lawal

Department of Chemical Sciences, Fountain University, Osogbo, Nigeria

ARTICLE INFO

Keywords:
Energy
Graphene
Composite
Metal oxide
Polymer

ABSTRACT

The purpose of the current review article is to present a comprehensive understanding regarding pros and cons of graphene related nanocomposites and to find ways in order to improve the performance of nanocomposites with new designs. Nanomaterials including GR are employed in industrial applications such as supercapacitors, biosensors, solar cells, and corrosion studies. The present article has been prepared in three main categories. In the first part, graphene types have been presented, as pristine graphene, graphene oxide and reduced graphene oxide. In the second part, nanocomposites with many graphene, inorganic and polymeric materials such as polymer/GR, activated carbon/GR, metal oxide/GR, metal/graphene and carbon fibre/GR have been investigated in more detail. In the third part, the focus in on the industrial applications of GR nanocomposite, including super capacitors, biosensors, solar cells, and corrosion protection studies.

1. Introduction

Composite materials are materials formed by combining two or more materials with different properties to produce an end material with unique characteristics. Composite materials are combination two or more materials to take advantage of the best properties and characteristics of each. Pristine graphene has a large surface area, excellent electron mobility and conductivity, and a wide electrochemical window but many researchers have shown that pristine graphene may not exhibit substantial advantages as an electrode material on its own, and to enhance electrochemical activity, desired functionality and electronic, it is necessary to introduce impurities (Ramakrishnan et al., 2015).

Graphene hybrid composites based on GR with inorganic nanostructures (Zhou et al., 2019).(Yan et al., 2015) (Altuntas et al., 2016; Bai et al., 2017; Chauhan et al., 2017), conducting polymer (Gokoglan et al., 2017; Liu et al., 2017a,b; Vinay Deep Punethaa, Sravendra Ranab et al., 2017; Wu et al., 2017) and organic materials (Yang et al., 2016) have been used for fabrication of electrochemical sensors for detection of biomolecules, electromagnetic absorbers, photovoltaic cells, photodiodes, supper capacitor and optical limiting devices.

Various research groups have reported the incorporation of graphene in nanocomposites and the resultant enhancements obtained in the mechanical strength as well as the electrical conductivity of the composites. These nanocomposites also typically exhibit enhanced thermal stability and electrochemical activity, as well as gas barrier properties. The presence of graphene in these composites improves the mechanical/electrical properties of biomaterials and increases cellular attachment and growth at biomaterials surface. Apart from that, the major advantage of these nanocomposites is that the positive changes occur even with a small amount of graphene filler and in the presence of a variety of polymeric matrices.

This review is to highlight the importance of graphene and its nanocomposites with polymer, active carbon, metal, metal oxide, carbon fibre and their applications.

1.1. Pristine graphene (GR)

GR represents a class of carbon materials based on a monolayer of carbon atoms arranged in a honeycomb lattice. As a novel single-atom-thick sheet of sp^2 hybridized carbon atoms, GR has attracted extensive attention in recent years because of its unique and remarkable properties, such as excellent electrical conductivity, large theoretical specific surface area, and strong mechanical strength. Its remarkable electronic, optical, mechanical, thermal, and electrochemical properties have made it a suitable electronic material for electrochemical sensing, as graphene has a very good electronically low-noise. It is produced most prominently the micromechanical cleavage of graphite, epitaxial growth on silicon carbide, chemical vapour deposition (CVD) of hydrocarbons on transition metal surfaces, as well as the dispersion of graphite in organic solvents, present difficulties in obtaining process able graphene sheets in large quantities thus impeding full exploitation of its exciting properties Fig. 1. Recently, GR has attracted an enormous amount of interest for its use in biosensors (Xie et al., 2016; Wang et al., 2017; Zhang et al., 2017; Zhao et al., 2017) in various transduction modes from electrical and electrochemical to optical detection (Arduini et al., 2016; Bahadır and Sezgintürk, 2016). GR's excellent fluorescence

E-mail address: lawal.abdulazeez@fuo.edu.ng.

https://doi.org/10.1016/j.bios.2019.111384
Received 15 March 2019; Received in revised form 27 May 2019; Accepted 29 May 2019
Available online 03 June 2019
0956-5663/

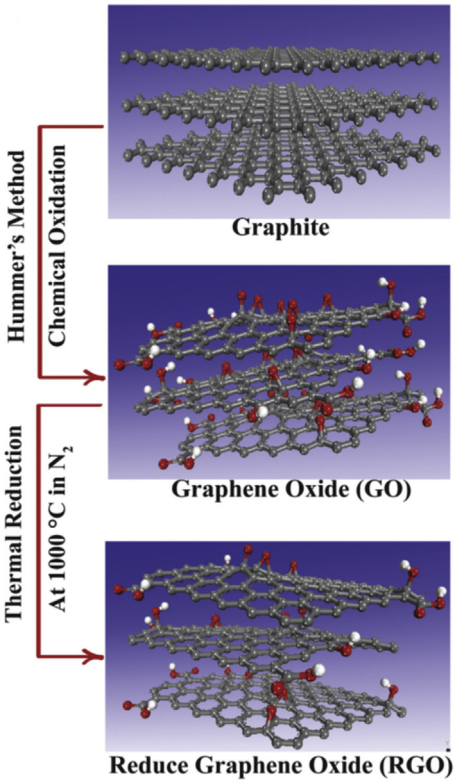

Fig. 1. Schematic of structure formation from graphite to RGO.

quenching ability has been exploited in optical sensors. Some of the exceptional properties of GR, its high electrical conductivity and their very efficient electrocatalytic behaviour are the most relevant for electrochemical applications. GR's unique advantages includes enhanced electronic properties, a large edge plane/basal plane ratio, and rapid electrode kinetics. GR-electroanalytical based electrodes have higher sensitivities, lower limits of detection, and faster electron transfer kinetics than traditional carbon electrodes. GR's high surface area, excellent electron conductivity, super hydrophobicity and enhanced mechanical strength of GR films, have made the research on GR films to blossom in recent decades and many biosensors have incorporated GR as sensing elements for biomolecular molecules (Boujakhrout et al., 2015; Cernat et al., 2015; Borisova et al., 2016).

Research groups are now carrying out exciting work using graphene and its composites in applications such as super capacitors (Oraon et al., 2016; V. Velmurugan*, U. Srinivasarao et al., 2016; Veeramani et al., 2016; Amin et al., 2017; Ahirrao et al., 2018; Qu et al., 2019), fuel cell (Marinoiu et al., 2018; Perveen et al., 2018; Arukula et al., 2019) (Baruah and Kumar 2018; Liao and Wu, 2019; Wang et al., 2019), batteries (Liu et al., 2015a,b,c; Du et al., 2018, Kumar et al., 2018; Gao et al., 2019; Hu et al., 2019; Liao and Wu, 2019; Wang et al., 2019), photocatalysis (An et al., 2013; Alomair and Mohamed, 2018; Sharma et al., 2018; Ton et al., 2018; Wang et al., 2018), photovoltaics (Dong et al., 2014), biosensors (Celik et al., 2015; Feng et al., 2015; Arduini et al., 2016; Raicopol et al., 2016; Chen et al., 2017; Gupta and Meek, 2018; Puiu and Bala, 2018; Wang et al., 2018), sensor (Tian et al., 2019), gas sensors (Achary et al., 2018; Chen et al., 2018), photonics, solar cell (Das et al., 2018; Giuri et al., 2018; Mehmood et al., 2018; Rahmawati et al., 2018; Timoumi et al., 2018; Gao et al., 2019), light-emitting diodes, laser, optoelectronics, photocatalyst (Hafeez et al., 2018; Jose et al., 2018; Kumar et al., 2018; Labhane et al., 2018; Mahvelati-Shamsabadi et al., 2018; Sephra et al., 2018; Xu et al., 2018; Jia et al., 2019; Qu et al., 2019), thin-film transistors (Zhang et al., 2014), memristive device (Aziz et al., 2019), tissue engineering and field effect transistor (FET) (Chen et al., 2013; Mukherjee et al., 2015; Pachauri and Ingebrandt, 2016; Siddique et al., 2017). Graphene oxide (GO) and reduced grapheme oxide (RGO) are oxidizing form of graphene and they are generally produced by exfoliation of graphite oxide. They are more popular than pristine graphene because they have better dispersion in water and they both have reactive oxygen group Fig. 1.

1.2. Graphene oxide (GO)

GO consists of a single-layer of graphite oxide and is usually produced by the chemical treatment of graphite through oxidation, with subsequent dispersion and exfoliation in water or suitable organic solvents. GO sheets can also be produced by a modified Hummers' method (Hummers and Offeman, 1958; Park et al., 2008). It is presumed that there are presences of various oxygen-containing functional groups in the GO Fig. 1. The oxygen functional groups have been identified as mostly in the form of hydroxyl and epoxy groups on the basal plane, with smaller amounts of carboxyl, carbonyl, phenol, lactone, and quinone at the sheet edges. The wide range of oxygen functional groups on both basal planes and edges of GO makes it to be readily exfoliated and functionalized to yield well-dispersed solutions of individual graphene oxide sheets in both water and organic solvents, thus its applications in nanocomposites (Zhao et al., 2018; Singu and Yoon, 2019; Xue et al., 2019; Yang et al., 2019), battery (Xiao et al., 2018; Kumar et al., 2019), photocatalysis (Akyüz and Koca, 2018; Jia et al., 2019), sensor (Guan et al., 2018; Jasmi et al., 2018; Ma et al., 2018) and capacitores (Aghazadeh, 2018). The oxygenated groups in GO can strongly affect its electronic, mechanical, and electrochemical properties. Hence they account for the differences between GO and pristine graphene. GO monolayers can be deposited in controllable density onto a large variety of substrates, thus enabling the preparation of thin conductive films on solid and flexible substrates which enhances its use as nanocomposites. Many researchers have used GO for fabrication of graphene nanocomposite while some researchers have investigated on GO with nanocomposites to enhance their mechanical, electrical and thermal properties:

Song et al. (Song et al., 2019) reported the preparation and application of GO/waterborne polyurethane (WPU) composite paste. They analysed rheological properties of GO/WPU composite paste, which were strongly affecting the printing pattern definition. They also investigated the influences of reduced GO (rGO)/WPU composite paste printed fabrics with various GO contents on UV protection factor (UPF) values and UV transmittance. The colour performance and fastness of rGO/WPU composite paste printed fabrics were evaluated. GO/WPU 0.9% composite paste possessed the lowest printing viscosity index (PVI) and excellent printing definition. In terms of UV protection, rGO/WPU composite paste printed fabrics with low GO loading still exhibited great UV protection ability, and super higher UPF value (7 5 7) was obtained at rGO/WPU 1.2% composite paste printed fabric. They increased the K/S values of rGO/WPU composite paste printed fabrics with the increase of GO content.

Sharma et al.(Sharma et al., 2019) synthesised a polymer nanocomposite Poly(methyl methacrylate)-Graphene Oxide (PMMA-GO) in the laboratory using in-situ free radical polymerization with varying concentrations of GO (0.5%, 1% PMMA), where GO was produced using Improved Hummers' method. They observed the effect of the nanocomposite on the pour point depression and rheological properties of an Indian waxy crude oil sample. The synthesized nanocomposite was evaluated as pour point depressant considering the improvement in the flow properties of the crude oil. Techniques such as FTIR, Raman and UV–visible spectroscopy, Field Emission Scanning Electron Microscopy (FESEM), Gel Permeation Chromatography (GPC) were used for the analysis of the synthesized nanocomposites and some of the techniques revealed the formation of PMMA-Graphene Oxide and the intermediate products.

Yaramandi et al. (Yarahmadi et al., 2018) chemically functionalised GO with starch, as a natural polymer, and added to the epoxy/amine

system. The cure kinetics of neat epoxy and its composites containing pristine and starch-functionalized GO (GO-St) were assessed using Differential scanning calorimetry while SEM was used to detect cryo-fractured surfaces of epoxy/GO and epoxy/GO-St nanocomposites.

Giuri et al. (Giuri et al., 2018) prepared GO by a modified Hummers' method and reduced by a green method based on UV treatment in inert atmosphere. UV–visible spectroscopy and X-ray photoelectron spectroscopy (XPS were used to monitored GO reduction and evaluating the change of absorption peak by monitoring the decrease of the oxygen groups linked to carbon. Spin coating on different substrates were also used to form nanocomposite films which were characterized by several techniques. .

1.3. Reduced graphene oxide (rGO)

rGO is prepared from graphene oxide through a two-step covalent modification approach. GO was first enriched with reactive epoxy groups by anchoring (3glycidyloxypropyl) trimethoxysilane at the hydroxyl groups located on the nanocarbon basal plane. Modified graphene oxide was further cross-linked and partially reduced by treatment with the fourth generation ethylenediamine core polyamidoamine G-4 dendrimer producing graphene nanoparticles with crumpled paper-like morphology. GO can also be reduced through thermal reduction of GO Fig. 1 and electrochemical reduction of GO Fig. 2.

Several researchers have used rGO for fabrication of graphene composite:

Araque et al. (Araque et al., 2013) employed rGO as a composite and as a coating material for glassy carbon electrodes and the nanostructured electrode was tested for the preparation of electrochemical biosensors by immobilizing the enzyme tyrosinase through cross-linking with glutaraldehyde. Tyrosinase showed excellent electro-analytical behavior for catechol with a fast response in about 6 s, linear range of 10 nM–22 mM, sensitivity of 424 mA M1, and low detection limit of 6 nM. The enzyme biosensor also showed high stability when stored at 4 C under dry and wet conditions.

Pathak et al. (Pathak et al., 2019) incorporated rGO into polyaniline. The rGO was synthesized and incorporated in different weight (0–0.5 wt%) fraction in dodecylbenzenesulfonic acid (DBSA) doped PANI-divinylbenzene (DVB) polymer to get PANI-DBSA/DVB nanocomposite. Universal testing machine (UTM) and transmitted electron microscopy (TEM) were used to analyse the mechanical and interfacial interaction. They found that the addition of optimum 0.3 wt % rGO improved flexural strength and modulus of PANI-DSBA/rGO-DVB composite by 153% and 32% respectively over neat PANI-DBSA/DVB nanocomposite. The maximum electrical conductivity 0.301 S/cm, glass transition temperature (Tg) and thermal stability of nanocomposite were realized at 0.3 wt % of rGO. Improvement of interfacial bonding by H-bonding and p-p interaction were confirmed using Raman spectroscopy and HRTEM.

Karachi et al. (Karachi et al., 2018) prepared nanocomposite material composed of rGO-supported rhodium nanoparticles (rGORhNP) by reducing graphene oxide with NaBH4 and Rh nanoparticles deposited in situ on the 2D carbon nanomaterial planar sheets. An optimal Rh loading of 18 wt% was observed, leading to the highest CH_4 formation rate (814.38 μmol CH_4.gRh T -1 h -1 at 175 °C) and quantum efficiency of 2.55%. The deleterious effect of H_2O formation during the reaction on the photocatalytic activity has been apparent and additional evidences confirmed that H_2O desorption was one of the reasons why the system needed heating.

Jose et al. (Jose et al., 2018) reported the synthesis of silver nanoparticles supported on graphene oxide sheets by a hydrothermal method. They grew silver nanoparticles on highly conducting rGO sheets, thereby preventing electron–hole pair recombination. The as prepared silver-decorated reduced graphene oxide nanocomposite was characterized by UV–Vis spectroscopy, X-ray diffraction, Raman spectroscopy, photoluminescence technique, scanning electron microscopy, high-resolution transmission electron microscopy, X-ray photoelectron spectroscopy and BET measurements. The photocatalytic ability of the prepared composite was evaluated against two dyes— indigo carmine and methylene blue—in the presence of sodium borohydride as an inducer.

Zabihi et al. (Zabihi et al., 2018) studied a nanocomposite–poly (methyl methacrylate) matrix material as a supercapacitor was presented. The study includes morphological, structural, and electrochemical characterization. Different electrolytes were used, for which both pseudocapacitance (for rGO) and electric double-layer capacitance (for functionalized graphene) were observed. An optimum nanocomposite weight percentage was found (2%), and the best performance with highest capacitance (30.4 F/g) was seen for the electrolyte including the smallest anions (OH_2), being among the best values for similar systems, that is, a nanocomposite/nonconductive polymer matrix.

Yang et al. (Yang et al., 2019) prepared rGO-Cu_2O nanocomposites with long-term antibacterial activities by reducing copper sulphate supported on GO using ascorbic acid as reducing agent in the presence of polyethylene glycol (PEG) and sodium hydroxide at room temperature. The rGO provided a protective barrier for Cu_2O, preventing Cu_2O from reacting with external solution to leach copper ions too quickly. rGO also promoted the separation of photoexcited charge carriers of Cu_2O nanoparticles to enhance the oxidative stress reactive and protected Cu_2O from falling apart in the phosphate buffered rGO large specific surface area improved the dispersibility of Cu_2O by electrostatic interaction. The rGO-Cu_2O nanocomposites resulted in the excellent antibacterial activities of against *Escherichia coli* (*E. coli*) and *Staphylococcus aureus* (*S. aureus*).

Lu et al. (Lu et al., 2018) presented a sandwich-structured SnS2@ Reduced graphene oxide (SnS2@rGO) nanocomposite consisting of SnS2 sheets uniformly anchored on both sides of rGO sheets. The SnS_2@ rGO nanocomposites, prepared through a dipping process combining with a hydrothermal method, show good electrochemical performance, including the high reversible capability of 959.2 mAh g^{-1} at 500 mA g^{-1} over 500 cycles, and superior rate performance. A SnS_2@ rGO nanocomposite is a promising anode candidate for practical application in Li ion batteries.

2. Graphene nanocomposite

Graphene's exceptional thermal, mechanical, and electronic properties, makes it stands out as the most promising candidate to be a major filling agent for composite applications. Numerous researchers have investigated on GR with nanocomposites to enhance the mechanical, electrical and thermal properties of nanocomposites.

Graphene nanocomposites electrodes containing GR/rGO and Iridium oxide (Kurbanoglu et al., 2017), Au nanostructures (Li et al., 2017; Saeed et al., 2017; Wu et al., 2017; Xu et al., 2017; Zhu et al., 2017), AgNP (Huang et al., 2015; Huang et al., 2015; Hui et al., 2015; Jamil et al., 2015; Yusoff et al., 2017), FeNP (Balamurugan et al., 2016; Teymourian et al., 2017; Yu et al., 2017), CeNP (Nayak et al., 2015; Du et al., 2017; Tian et al., 2017), PtNPs (Liu et al., 2015a,b,c; Liu et al., 2015a,b,c; Sun et al., 2015; Zan et al., 2016), Pd–Pt NPs (Mijowska et al., 2015; Xi et al., 2016), TiO_2 NPs (Liu et al., 2017a,b,c; Liu et al., 2017a,b,c) (Muthuchamy et al., 2017), CuO_2 NPs (Wu et al., 2016), ZrO2 NPs (Mogha et al., 2016) and ZnO (Sandhya et al., 2018) have been used as electrochemical biosensors for the detection of biomolecules. These resulting nanocomposites often exhibit superior surface area and electrical conductivity, less biofouling and improved sensitivity compared to pristine GR.

2.1. Graphene-polymer nanocomposite (GR/P)

GR/conducting polymer composites have been synthesized by either in situ chemical or electrochemical polymerization of monomers in the

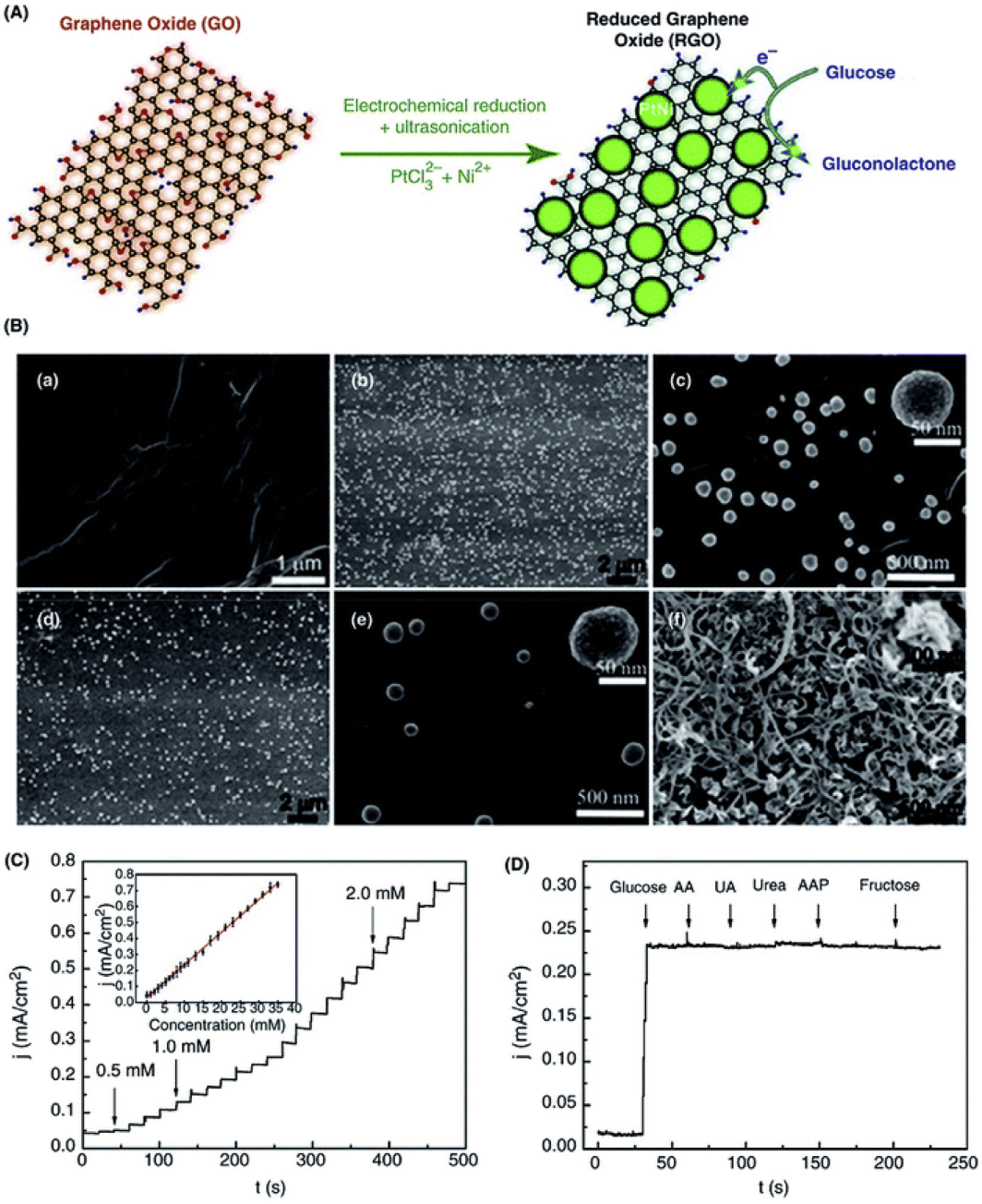

Fig. 2. (A) Schematic representation of the formation of PtNiNPs/rGO nanocomposites by electrochemical reduction method. (B) SEM images of the GO nanosheet, PtNiNPs/ERGO, PtNi NPs/CRGO nanocomposites and PtNiNPs/SWCNTs nanocomposites. (C) Amperometric response of PtNiNPs/ERGO/GCE after adding 0.5, 1.0, and 2.0 mM glucose and the calibration curve (inset). (D) Influence of interfering bioanalytes including 0.5 mM ascorbic acid (AA), 0.1 mM uric acid (UA), 0.1 mM urea, 0.5 mM AAP, and 0.5 mM fructose to 5.0 mM glucose at the PtNiNPs/ERGO/GCE. Here, electrochemically and chemically reduced GO are ERGO and CRGO, respectively. [Reprinted with permission from H. Gao, F. Xiao, C. B. Ching and H. Duan, One-Step Electrochemical Synthesis of PtNi Nanoparticle-Graphene Nanocomposites for Nonenzymatic Amperometric Glucose Detection, ACS Appl. Mater. Interfaces, 2011, 3, 3049–3057. Copyright© American Chemical Society.].

presence of GR. GR/P nanocomposites prepared by combining the vast πconjugated system of conducting polymers with GR have been researched (Olean-Oliveira and Teixeira, 2018). Inclusion of nano filler such as graphene within the polymer host has potential application in biosensors, energy storage devices, photo catalysts, drug delivery. Recently, a variety of processing routes have been reported for dispersing both GNP and GO-derived fillers into polymer matrices. The fabrication of polymer-graphene nanocomposite has been facilitated by the use of ultrasonication process for the dispersion of nanofiller, however the controlled amount of weight % and size of the nanomaterial is carefully taken into consideration (Sharma et al., 2018). A majority of graphene/polymer composites investigated are fabricated using GO, chemically reduced graphene oxide (CRGO), or thermally reduced graphene oxide (TRGO) as fillers Fig. 2 Table 1. Three-dimensional (3D) graphene-based polymer nanocomposites (3D-GPNCs) are considered as new generation materials for various multi-functional applications. In recent years, several research groups have developed graphene-polymer nanocomposite:

Guan et al. (Guan et al., 2018) presented an overview of the preparation, properties and applications of 3D-GPNCs. Three main approaches for fabricating 3D-GPNCs, namely 3D graphene based template, polymer particle/foam template, and organic molecule cross-linked graphene, were introduced. They performed and discussed a thorough investigation and comparison of the mechanical, electrical

Table 1
Values of the lowest electrical percolation thresholds and maximum electrical conductivities which have been reported in the literature for GNP and graphene-based nanocomposites for selected polymer matrices.

Matrix polymer	Filler type	Lowest percolation threshold reported (wt%)	Filler type	Maximum conductivity (S/cm)[a]	Ref.
Epoxy	Funct. EG	1.0	RG–O	~0.05 (19 wt%)	
Nylon-6	GO	0.5	GO	8.4×10^{-3} (1.8 wt%)	
Poly(aniline) (doped)	GNP	0.7	GNP	522 (10 wt%)	(Arukula et al., 2019.), (Salimikia et al., 2018) (Farajvand et al., 2018)
Polycarbonate	TEGO	0.3	TEGO	0.5 (4.8 wt%)	
Poly(ethylene)	RG–O	0.2	RG–O	0.1 (1.3 wt%)	
Poly(ethylene terephthalate)	TEGO	1.0	TEGO	0.02 (6.5 wt%)	
Poly(methyl methacrylate)	GNP	0.7	GNP	~1 (10 wt%)	
Poly(propylene)	GNP	0.7	GNP	5×10^{-3} (10 wt%)	
Poly(styrene)	Funct. G–O	0.2	RG–O	0.15 (2 wt%)	
Poly(vinyl alcohol)	RG–O	0.5	RG–O	0.1 (7.5 wt%)	
Poly(vinyl chloride)	GNP	1.4	GNP	0.06 (14.8 wt%)	
Poly(vinylidene fluoride)	TEGO	2.0	TEGO	3×10^{-4} (4 wt%)	
Polyurethane[b]	TEGO	0.6	TEGO	N/A (3.6 wt%)	
Polypyrrole					132

and thermal properties of 3D-GPNCs. They reviewed various potential applications of 3D-GPNCs, including energy storage and conversion, electromagnetic interference shielding, oil/water separation, and sensors.

Salimikia et al. (Salimikia et al., 2018) prepared a solid-phase microextraction fibre by polyaniline/graphene oxide nanocomposite as sorbent on the surface of a platinized stainless steel wire using electrospinning technique. The nanocomposite structure was characterized by SEM and FTIR and used for determination of nicotine The limit of detection of nicotine, linear dynamic range, intraday and inter-days precisions were found to be $0.01\,mg\,g^{-1}$, $0.05–700\,\mu g\,g^{-1}$ (R2 = 0.996), 6.9 and 8.1%, respectively.

Farajvand et al. (Farajvand et al., 2018) synthesised Grapheneoxide/polyaniline nanocomposite through chemical method and then the graphene oxide/polyaniline nanocomposite was characterized by using XRD, FESEM, FTIR and TGA techniques. Grapheneoxide/polyaniline composite was investigated as an adsorbent in the presence of chelating dithizone ligand to measure cadmium (II) ions in aqueous media. The analytical figure of merit such as limit of detection ($0.1\,\mu g\,L^{-1}$), limit of quantification ($0.4\,\mu g\,L^{-1}$), linear dynamic range ($0.4–1000\,\mu g\,L^{-1}$), repeatability (%1.3), enrichment factor (210) and relative recovery percentage (99%), were obtained for cadmium (II) spike aqueous samples.

Suvina et al. (Suvina et al., 2018) studied the formation of novel hydrogels of conjugate polymer polypyrrole (PPy) and rGO composite as heavy metal sensors for the simultaneous detection of four different metal ions such as Cd^{2+},Pb^{2+},Cu^{2+} and Hg^{2+}. PPy-rGO hydrogel composite exhibits very high surface area of $21.48\,m^2\,g^{-1}$, which is almost 3.5 times higher than that of PPy ($5.89\,m^2\,g^{-1}$).

2.2. *Graphene/activated carbon nanocomposite GR/AC*

Activated carbon has been at the centre of research and commercial utilization, based on low cost, wide availability and relatively good performance due to its high surface area and advantageous pore structure. Adsorption properties of GR/AC to metal ions have been reported and several methods have been developed to prepare graphene/activated carbon nanosheet composite as high-performance electrode material for supercapacitors.

In recent years, several research groups have used activated carbon for fabrication of graphene composite:

Lu et al. (Lu et al., 2018) described a facile method to synthesize a new type of catalyst by electrodepositing Agnanocrystals (AgNCs) on the different polymer dyes, Poly (methylene blue) (PMB) or Poly (4-(2-Pyridylazo)-Resorcinol) (PAR) modified graphene carbon spheres (GS) hybrids. The self-assembled GS take dual advantages of carbon spheres and graphene composite was used as electrochemical non-enzymatic sensor for H_2O_2 detection. They found that the proposed electrodes, especially for Ag/PMB/GS/GCE, displayed a peculiar electrocatalytic activity towards H_2O_2 reduction synergistically as compared to Ag/PAR/GS/GCE or Ag/GS/GCE alone. Ag/PMB/GS/GCE showed a linear response over the H_2O_2 concentration range of 0.5–1112 μM. The detection limit and sensitivity is 0.15 μM and $400\,\mu A mM^{-1}\,cm^{-2}$, respectively.

Xin et al. developed a novel carbon composite material consisting of graphene and activated carbon (G/AC) for the oxygen electrode (cathode) in Li-ion batteries. In the G/AC, the graphene forms a three-dimensional (3D) network with good electrical conductivity and excellent mechanical strength and flexibility, while the AC layer on the graphene surface provides numerous meso/micropores with diameters of less than several nanometers that act as active sites (or nucleation sites) for the discharge reaction. The particle size of the discharge product Li_2O_2 becomes much smaller (~10 nm), and the particles are distributed more homogeneously in the G/AC cathode, whereas toroidal particles as large as 100–200 nm occur in the pristine graphene cathode. The charge voltage for the G/AC cathode gradually increases from ~3 V–4 V, while the voltage for the graphene cathode shows a steep increase to a plateau at 4.2–4.3 V and eventually exceeds 4.5 V.

Zheng et al. (Zheng et al., 2014) developed a simple method to prepare graphene/activated carbon (AC) nanosheet composite as high-performance electrode material for supercapacitor.

Glucose solution containing dispersed GO sheets is hydrothermally carbonized to form a brown char-like intermediate product, and finally converts to porous nanosheet composite by two-step chemical activation using KOH. The composite has a relatively high packing density of $\sim 0.3\,g\,cm^{-3}$ and large specific surface area of $2106\,m^2\,g^{-1}$, as well as containing plenty of mesopores. It exhibits specific capacitance up to 210 F/g in aqueous electrolyte and 103 F/g in organic electrolyte, respectively, and the specific capacitance decreases by only 5.3% after 5000 cycles.

Hossain and Park, (2016) applied a hydrothermal technique to synthesize glucose-treated reduced graphene oxide-activated carbon (GRGO/AC) composites. Platinum nanoparticles (PtNP) were electrochemically deposited on the modified GRGO/AC surface, and chitosan-glucose oxidase (Chit-GOx) composites and Nafion were integrated onto the modified surface of the working electrode to prepare a highly sensitive glucose sensor. The fabricated biosensor exhibited a good amperometric response to glucose in the detection range from 0.002 mM to 10 mM, with a sensitivity of 61.06 μA/mMcm^2, a short response time (4 s) and a low detection limit of 2 μM (signal to noise ratio is 3). Glucose levels in human urine were tested in order to conduct a practical assessment of the proposed sensor, and the results

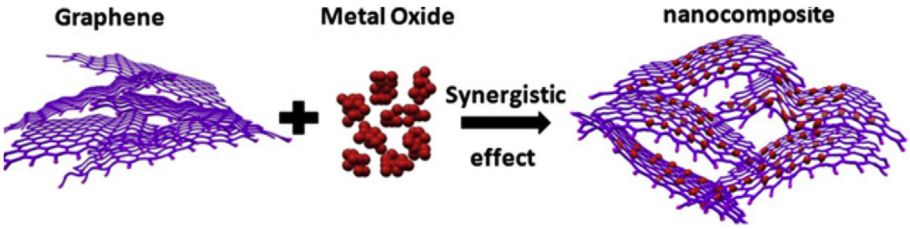

Fig. 3. A general wet-chemistry strategy to fabricate graphene/metal oxide composites.

indicated that the sensor had superior urine glucose recognition.

2.3. Graphene/metal oxide nanocomposite (G/MOs)

Metal oxides are used as pseudocapacitive electrode materials for supercapacitors because of their high-energy density. G/MOs has attracted a lot of attention as anode materials for SIBs due to high kWh/cost and G/MO nanocomposite is an efficient high-performance electrode material in an electrochemical supercapacitor. Most of the existing methods of the composite preparation, constituents were separately prepared and mixed or external aids were employed for the production of composites, which has many limitations in large-scale synthesis Figs. 3–7, In recent years, several research groups have used metal oxide for fabrication of graphene nanocomposite:

Abdulmuain et al. (u7/Abd Muain, Cheo et al., 2018) demonstrated that the immobilization of HBcAg onto the gold nanoparticles-decorated reduced graphene oxide (rGO-enAuNPs) nanocomposite could be used as an antigen-functionalized surface to sense the presence of antiHBcAg. The modified rGO-en-AuNPs/HBcAg was then allowed to undergo impedimetric detection of antiHBcAg with anti-estradiol antibody and bovine serum albumin as the interferences. The electrochemical response showed a linear relationship between electron transfer resistance and the concentration of anti-HBcAg ranging from 3.91 ng mL^{-1} to 125.00 ng mL^{-1} with lowest limit of detection (LOD) of 3.80 ng mL^{-1} at 3 σm $^{-1}$. This established method exhibits potential as a fast and convenient way to detect anti-HBcAg.

Othmen et al. (Ben Haj Othmen, Hamdi et al., 2018) hybridized Iron-doped tin oxide nanoparticles (Fe-doped SnO2 NPs), with different iron concentrations and rGO through a three steps elaboration method to obtain Fe-doped SnO_2/rGO nanocomposite. The composite was characterised by XRD, TEM, XPS, Rahman spectroscopy and FTIR.

Beura et al. (Beura and Thangadurai, 2018) synthesised ZnO-graphene by hydrothermal method. Band gap energy of the composite has decreased from 3.12 to 2.84 eV, while the photoluminescence lifetime has increased from 15.05 to 21.60 ns with Sn ion doping. Composite photocatalytic activity was tested on anionic dyes (methyl orange, methyl Orange (MO) and methyl red) and cationic dyes (methylene blue and rhodamine-B) under UV light. The MO was additionally tested under direct sunlight irradiation. Maximum degradation of MO was obtained to be 89.3 and 99.1% under UV and sunlight irradiation respectively, that are 9 and 8% higher than the same shown by undoped ZnO-graphene composite. The photocatalyst could effectively photodegrade anionic dyes in acidic medium and cationic dyes in basic medium as dictated by the type of charges on their surface induced by the pH of the media.

Borah et al. (Borah et al., 2018) reported the synthesis of in-situ TiO2/rGO nanocomposite and used as a heterogeneous catalyst for the transesterification of waste cooking oil into biodiesel. The prepared catalyst was characterised viz. XRD, FT-IR, SEM, EDX, Transmission TEM, TGA techniques confirming the successful formation of nanocomposite. The catalyst showed good catalytic activity in biodiesel production and biodiesel conversion of 98% was obtained under optimum reaction conditions. Biodiesel conversion was confirmed by Proton Nuclear Magnetic Resonance (1H NMR), Carbon Nuclear Magnetic Resonance (13C NMR) and Gas Chromatography-Mass Spectroscopy (GC-MS) techniques. The excellent catalytic activity of TiO_2/rGO could be attributed to the enhanced surface area of the composite.

Botcha et al. (Botcha et al., 2018) improvised modified Langmuir-Blodgett (MLB) technique and extended to transfer GO-Cu_2O nanocomposite monolayer sheets, by introducing Cu^{2+} ions into the subphase at room temperature. The nanocomposite was characterised using XPS, TEM, and Raman spectroscopy. Based on Raman, XPS and TEM studies it has been confirmed that heat treatment at 400 °C in vacuum results in the formation of agglomerated Cu nanoparticles of size (23 ± 9) nm distributed uniformly over rGO sheets. The electrical characterization of nanocomposite sheets on SiO_2/Si in back-gated FET geometry revealed that the electrical conductivity of as-transferred GO-Cu_2O sheets was similar to that usually observed for GO monolayer sheets.

Chen et al. (Chen et al., 2018) synthesized a Two-dimensional MnO_2/rGO nanocomposite by a facile wet chemical method at low temperature. Ultrathin layered MnO_2 nanosheets were well-dispersed and tightly attached on the surface of rGO sheets. Owing to a special laminar structure and higher electrical conductivity of rGO, the lithium ion diffusion and the electronic transport into the MnO_2/rGO nanocomposites were increased, resulting in improved electrochemical performance as a cathode material in lithium-ion batteries. The first discharge-specific capacity of the layered MnO_2/rGO nanocomposites is 279.7 mAh g^{-1} and maintains at 242 mAh g^{-1} after 60 cycles at 0.1C. The rate capability of MnO_2/rGO nanocomposites is 236.9, 230.2, 190.3, 159.7 and 121.4 mAh g^{-1} at 0.1C, 0.2C, 0.5C, 1C and 2C, respectively. The excellent electrochemical performances highlight the two-dimensional layered MnO_2/rGO nanocomposites as a potential cathode material of lithium-ion batteries.

Chou et al. (Chou and Wang, 2018) developed a highly stable, transparent, and a flexible composite electrode using rGO/silver nanowires (AgNWs)/Ga-doped zinc oxide (GZO) composite thin films. The rGO film was the first spin coated on flexible substrates and used as an adhesion enhancement layer. The AgNWs, which were used as a primary conductor, formed a random percolating network embedded

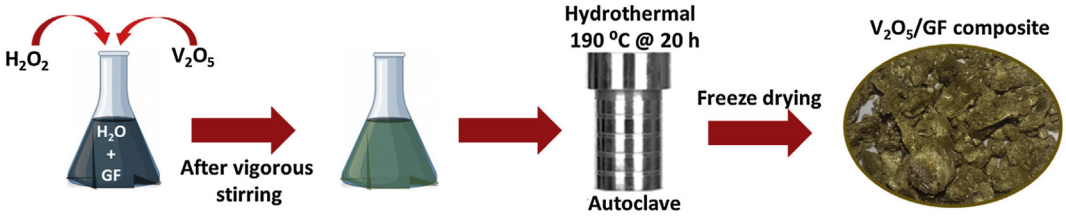

Fig. 4. Schematic of the synthesis process of V2O5/GF composite.

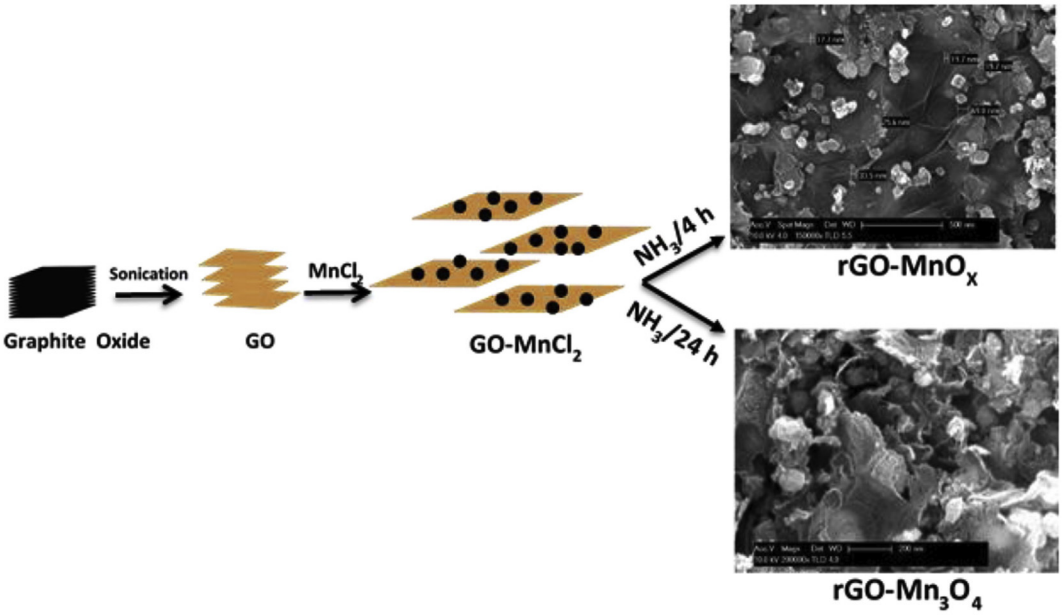

Fig. 5. Graphical representation of the synthesis of rGO-MnOx and rGO-Mn3O4 nanocomposites.

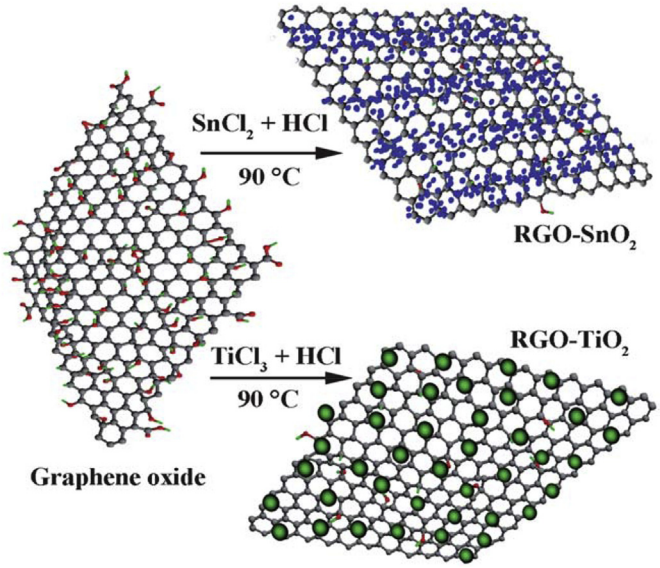

Fig. 6. A scheme showing the preparation of samples RGO–SnO2 and RGO–TiO2.

between the rGO and GZO films. The GZO film was sputtered on the surface of the AgNWs and was used as a protective layer to prevent the oxidation of the AgNWs. The rGO/AgNWs/GZO composite thin film exhibited excellent electrical conductivity and superior stability to a monolayer or a bilayer TCF. The sheet resistance of the composite film (5.45 ± 0.41 Ω/m) slightly increased to no more than 5% when exposed to the atmosphere for 60 days. The rGO/AgNWs/GZO composite film exhibited an optical transmittance of approximately 85% at a wavelength of 550 nm. A bending test was conducted for 600 cycles with a curvature radius of 1 cm, and the test results revealed that sheet resistance of the composite film varied by less than 10%.

Dargahi et al. (Dargahi et al., 2018) fabricated TiO_2-rGO composite through UV-assisted photocatalytic reduction of the graphene oxide. The XRD, FESEM, EDX, and FTIR analyses were implemented for characterization of the TiO_2, 1 at % Mo-doped TiO_2, and 1 at % Mo-doped TiO_2/rGO powders. Linear sweep voltammetry, amperometry, and electrochemical impedance spectroscopy tests were used to study the photoelectrocatalytic behaviour of the composite.

Gulati et al. (Gulati et al., 2018) obtained rGO@CuO nanocomposites by the impregnation of micrometer-sized malachite spheres, as a renewable and sustainable copper mineral precursor, on the GO sheets followed by calcination at 300–450 °C for 5 h rGO@CuO composites were found to be efficient and robust nanocatalysts compared with CuO nanoparticles (NPs) alone. This method offers several advantages, such as wide substrate scope, and avoids the usage of excess equivalent of substrates with minimal waste generation (E-factor = 0.24) and high reaction mass efficiency (80.7%).

Wang et al. (Wang et al., 2019) provided a comprehensive summary of the research development on the low-cost metal oxides/graphene composites (MOs/G) as anode materials for SIBs. They discussed the correlation of the morphological and structural properties of the composite materials with their performance in SIBs.

Huang et al. (Huang et al., 2017) synthesised The 3D NiO hollow sphere/rGO composite according to the coordinating etching and precipitating process by using Cu_2O nanosphere/GO) composite as template. The morphology, structure, and composition of the materials were characterized by SEM, TEM, HRTEM, XPS, and Raman spectra, and the electrochemical properties were studied by CV, EIS, and amperometry. The 3D NiO hollow sphere/rGO composite was used as glucose sensor and the modified electrode exhibits high sensitivity of $\sim 2.04\ mA\ mM^{-1}\ cm^{-2}$, quick response time of less than 5 s, good stability, selectivity, and reproducibility.

Yuan et al. (Yuan et al., 2016) fabricated Fe_2O_3/rGO composite (FFGC) by a hydrothermal method for the exploration of electrochemical energy storage, where the Fe_2O_3 nanoparticles (NPs) loaded onto the surface of rGO sheet uniformly. TEM of the composite image showed that visible micro-cracks were appeared on the surface of flower-like Fe_2O_3 NP, which did not interfere with its stably crystalline structure. FFGC was used as anode material for lithium-ion battery (LIB) as well as electrode material for supercapacitor (SC). The specific discharge capacity was of 1366 mAh g^{-1} at 0.1 A g^{-1} in LIB case, while the specific capacitance of 318.9 F/g at 0.1 A g^{-1} in SC experiment.

2.4. Graphene/metal nanocomposite

Metals such as Cu, Au, Fe, Ce etc., have been incorporated into graphene as composite for various applications such as sensing and imaging Fig. 8. With the success of graphene—metal nanoparticles

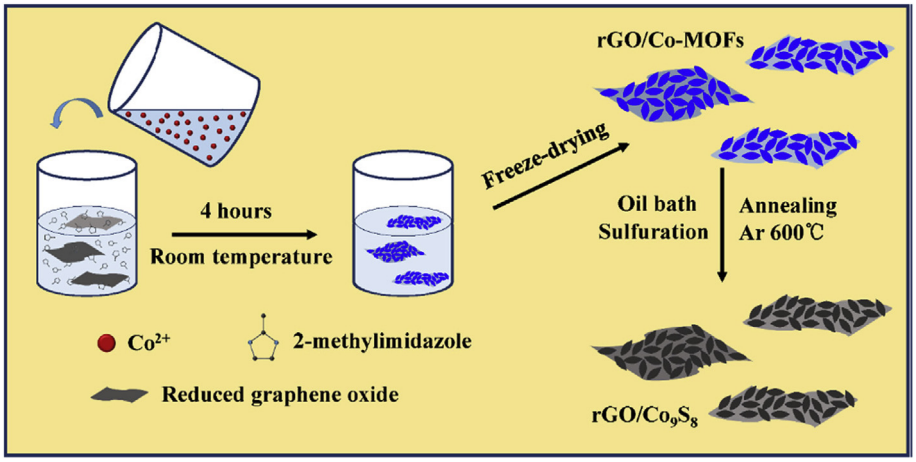

Fig. 7. Schematic illustration of the synthetic route for the fabrication of rGO/Co9S8.

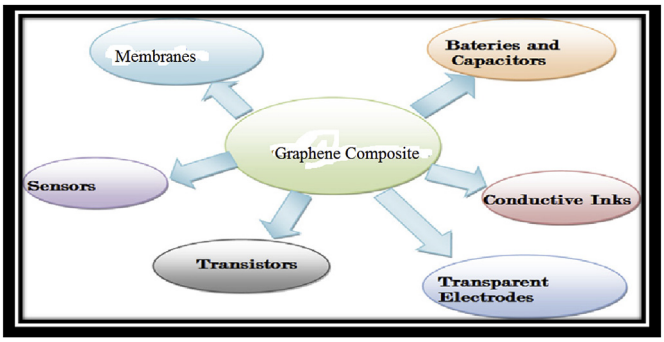

Fig. 8. Potential applications of graphene in different sectors ranging from conductive inks to chemical sensors, light emitting devices, energy, touch panels and high frequency electronics.

(NPs), its more recently discovered counterpart, graphene—metal nanoclusters (NCs) has gained prominence in the field of material science.

Nanocomposite with a room-temperature ultra-low resistivity far below that of conventional metals like copper is considered as the next generation conductor. However, many technical and scientific problems are encountered in the fabrication of such nanocomposite materials at present. In recent years, several research groups have used metals for fabrication of graphene composites:

Huang et al. (Huang et al., 2018) reported the production of a metal-organic framework-derived Co_9S_8 nanoflake on reduced graphene oxide sheet composites as an advanced sodium-ion battery anode Fig. 7. Using a galvanostatic intermittent titration technique, they revealed that the sodium diffusion coefficient of the composite is higher than that of its counterpart. rGO/Co_9S_8 composite electrode deliver a high discharge capacity of 551 mA h g^{-1} at 0.1 A g^{-1}, a good rate capability at 10 A g^{-1}, and an excellent cyclic stability up to 500 cycles. rGO/Co_9S_8 shows potential for practical applications in $Na_3V_2(PO_4)_3$krGO/Co_9S_8 full cells.

Arukula et al. (Arukula et al., 2019) reported a wet reflux strategy for the synthesis of rGO/polyaniline (PANI)/Pt–Pd composite, which was exploited as a potential anode catalyst with enhanced methanol oxidation capacity for direct methanol fuel cells (DMFCs). The constructed rGO/PANI/Pt–Pd composite was characterised using transmission electron microscope (TEMTEM). rGO/PANI/Pt–Pd features include active carbon support, extended architecture of electron conducting channels and number of methanol oxidation centres endows excellent DMFC power density of 117.45 mW cm^{-2} and concrete cell durability over 70 h.

Xuan et al. (Xuan et al., 2018) developed patterned 3D porous laser-induced graphene silver nanocomposite. The fabricated composite electrode exhibited a high, uniform electrical conductivity even under mechanical deformations. Addition of platinum and gold nanoparticles (PtAuNP) on the 3D porous LIG greatly improved the electrochemical performance for wearable glucose sensor applications. The fabricated glucose sensor exhibited low detection limit (5 μM), and acceptable detection range from 0 to 1.1 mM (covers the glucose range in sweat), and high linearity (0.99). In addition, the fabricated pH sensor also exhibited a linear response (66 mV/pH) at the range from 4 to 7.

Chen et al. (Chen et al., 2013) developed metal–organic framework (MOF) as the sensing platform. N,N-Bis(2-hydroxy-ethyl)dithiooxamidatocopper(II)(H_2d to a Cu) was chosen as the example MOF, because it strongly chemisorbs the dye-labeled probe TFO (triplex-forming oligonucleotide), and quenches fluorescence from the dye. The enhanced fluorescence signal has a relationship with the ds-DNA concentration, the detection limit is as low as 1.3 nmol L1 (S/N ¼ 3) with good selectivity, which is lower than that based on a graphene oxide platform and electrochemical-DNA sensor.

Zheng et al. (Zheng et al., 2018) reported the rapid and efficient fabrication and characterization of a novel nitrogen-doped graphene copper nanocomposite. It possesses an electrical resistivity of 0.16 μΩ cm at room temperature, far lower than that of copper. The composite has superior thermal conductivity (538 W/m·K at 25 °C) which is 138% of copper.

Zang et al. (Zang et al., 2018) prepared a nanocomposite consisted of copper nanowires (Cu NWs), metal-organic frameworks (MOFs) and GO by an easy and convenient functionalization way through direct ultrasound mixing. Morphology and size of the composite were characterized by SEM and TEM. Good electrochemical performance was observed with CV and amperometric i-t curve. The composite used as sensor showed a wide linear range (20 mMe26.6 mM) and a low detection limit of 7 mM (S/N ¼ 3) at applied potential of þ0.3 V (vs. Ag/AgCl). The selectivity was investigated against lactose, fructose, sucrose, maltose, xylose, and satisfactory anti-interference performance to acetaminophen, ascorbic acid, and uric acid was, tested in concentrations even higher than the normal physiologic levels.

Liu et al. (Liu and Guo, 2018) prepared a composite by facile chemical deposition of Cu nanospheres (CuNSs) on SH-β-CD functionalized reduced graphene oxide (SH-β-CD-rGO). The SH-β-CD-rGO/CuNSs nanocomposite was characterised by UV–vis, FT-IR, TEM, and CV. The composite was used for rapid and sensitive electrochemical method for the determination of trace 4-NP in water. The constructed electrochemical 4-NP sensor based on SH-β-CD-rGO/CuNSs demonstrates speediness, good sensitivity, wide linear range (0.05–25 μM and 25–100 μM) and low limit of detection (20 nM).

Gupta et al. (Gupta et al., 2018) reported the production of copper oxide/reduced graphene oxide nanocomposite. The catalyst used can

easily be recycled and reused in seven consecutive runs without compromising the product yields. Other notable advantages include using H_2O as a reaction medium and obtaining good to excellent yields.

Liu et al. (Liu et al., 2016) described the fabrication of Cu-graphene composite by immobilizing copper nanoparticles (Cu NPs; 20 nm) on GO sheets via in-situ reduction of copper(II) on a polydopamine (PDA) coating on a glassy carbon electrode. The modified electrode, used as H_2O_2 sensor, best operated at a working voltage of −0.4 V (vs. Ag/AgCl), has a linear response to H_2O_2 in the 5 μM to 12 mM concentration range, a sensitivity of 141.54 μAmM1cm^2, a response time of 4 s, and a 1.4 μM detection limit (at an S/N ratio of 3). The method was applied to the determination of H_2O_2 in sterilant by the standard addition method and gave recoveries between 97% and 99%.

Bagheri et al. (Bagheri et al., 2015) described a versatile method for fabrication of a H_2O_2 sensor by immobilizing copper nanoparticles (Cu NPs; 20 nm) on GO sheets via in-situ reduction of copper(II) on a polydopamine (PDA) coating on a glassy carbon electrode. The PDA film with its amino groups and catechol groups acts as both a reductant and an adhesive that warrants tight bonding between the Cu NPs and the support. The modified electrode, best operated at a working voltage of −0.4 V (vs. Ag/AgCl), has a linear response to H_2O_2 in the 5 μM to 12 mM concentration range, a sensitivity of 141.54 μAmM1cm^2, a response time of 4 s, and a 1.4 μM detection limit (at an S/N ratio of 3). The sensor is highly reproducible and selective (with minimal interference to ascorbic acid and uric acid). The method was applied to the determination of H_2O_2 in sterilant by the standard addition method and gave recoveries between 97% and 99%.

2.5. Graphene/fibres nanocomposite

Direct covalent bonding were mostly used by various researchers to graft graphene onto carbon fibre to form a GR/CF reinforcing structure:

Davoodi et al. (Davoodi et al., 2018) prepared a nanocomposite substrate from poly lactic acid (PLA) and GO using electrospinning method. Determining the possible placement of graphene oxide nanosheets in the electrospun fibre mats is the main goal of this work. The characterisation methods employed include SEM, AFM micrographs, tensile modulus and attenuated total reflectance Fourier-transform infrared spectroscopy (ATR-FTIR). They performed the study of the mechanical properties, surface chemical structure and topology of obtaining nanofiber mats.

Jasmin et al. (Jasmi et al., 2018) synthesised Polyurethane-graphene (PU-graphene) nanocomposite which was utilized as the sensing material for FBG temperature sensor. The nanocomposite was characterized using FTIR, TGA, SEM and EIS to study the morphology and physical properties of the materials for FBG temperature sensing application. FTIR shows that the strong intermolecular interaction between –O–C = O (ester) and hydrogen in graphene in PU-graphene was indicated by the shift to lower wavenumber of ether (C–O–C) peak at ~1220 cm^{-1} to ~1218 cm^{-1}. TGA shows the thermal stability of PU increases to 217 °C due to the strong intermolecular interaction with the presence of graphene flakes. EIS shows a good electrical conductivity of 1.39 × 10-9 Scm^{-1} in PU-graphene due to the electron transfer provided by graphene. SEM shows a rough and uneven texture on the surface of FBG coated by PU-graphene nanocomposite which shows that graphene flakes are completely coated by polyurethane polymer.

Jin et al. (Jin et al., 2018) reported a facile process for the hybridization of polyaniline nanofibers (PANI NFs) on functionalized reduced graphene oxide (FrGO) films by filtering the hybrid suspension of GO and in-situ polymerised PANI NFs followed by hydrothermal treatment to reduce GO and sulphur functionalisation of rGO. The as-prepared PANI NFs/FrGO composite films were uniform, flexible and stable with a high specific capacitance of 692.0 F/g at 1 A g^{-1} and excellent capacitance retention of 53.5% at 40 A g1. Using the composite films as electrodes exhibited a high capacitance of 324.4 F/g at 1 A g^{-1} and an energy density ~16.3 Wh kg^{-1} at a power density of 300Wkg1, showing a great promising in the applications for portable power and flexible supercapacitor.

Li et al. (Li et al., 2018) reported a vibration-powered micro-generator, based on electrospinning polyvinylidene fluoride (PVDF)/graphene oxide (GO) composite nanofiber film. With the help of the electrospinning process, the PVDF nanofibers chemically wrapped by GO lamellae, in which the polar β-phase nanocrystals are formed and uniaxially self-oriented by the synergistic effect of mechanical stretching, high-voltage alignment, and chemical interactions. The special core-shell structure formed during electrospinning process gives nanofiber better piezoelectric properties.

Wan et al. (Wan et al., 2018) reported the construction of a ternary flexible nanocomposite of bacterial cellulose/graphene/polyaniline (BC/GE/PANI) via a facile two-step strategy. The composite BC/GE/PANI has an electrical conductivity of 1.7 ± 0.1 S/cm, which is higher than most of PANI-based composites. It is believed that the BC/GE/PANI nanocomposite possesses great potential for applications in electromagnetic shielding and flexible electrodes.

3. Usage of graphene composite in industrial applications

Graphene nanocomposite has a great number of applications including engineering, electronics, medicine, energy, industrial, household design, and many more Fig. 8.

3.1. Lithium-ion and sodium-ion batteries

The rapid depletion of fossil fuels and environmental concerns has caused an ever-growing demand for technologies of advanced energy storage. The ever increasing demands for portable electronic devices, electric vehicles and hybrid electric vehicles (EVs/HEVs) have greatly stimulated the development of lithium-ion batteries (LIBs).Among the various energy storage systems, LIBs is considered a promising candidate for the effective storage of energy due to its' their high energy density and long cycle life. Rechargeable LIBs with high specific capacity, large power density, and long cyclic life are promising power sources for electric vehicles (Zhang et al., 2018). Sodium-ion batteries (SIBs) have been considered as a promising alternative to LIBs because sodium as an alkaline metal shows an electrochemical behaviour similar to that of lithium; sodium has abundant resources and low cost (Huang et al., 2018). Therefore, the charge storage mechanisms for sodium and lithium are expected to be similar. More importantly, Na is abundant in the earth crust and is thus cheaper. Due to the abundance of sodium sources and relatively high safety, SIBs are considered as a promising candidate for next-generation large-scale energy storage systems. However, currently the lack of suitable anode materials is limiting the development of SIBs. Metal oxides (MOs) which have the advantage of rich material sources and high theoretical capacity have attracted lots of attention as anode for SIBs in scientific community. Graphene oxide and reduced graphene oxide have been used in batteries. These materials are attractive because of their high specific surface area, low electrical resistance, low mass density, and high cyclic stability.

In recent years, several research groups have produced and explored the use of graphene nanocomposite in Lithium and Sodium-ion batteries:

Ko and Kim (Ko and Kim et al., 2018) constructed nanocomposites comprising reduced graphene oxide to further enhance rate capability Li/Na batteries. In both Li- and Na-ion electrolytes, the nanotube–reduced graphene oxide nanocomposite exhibits pseudocapacitive behaviour, indicated by broad voltammetric features and sloping charge-discharge voltage profiles under galvanostatic mode. This corresponding charge-storage process supports high capacities of 170 and 80 mAh g^{-1} in a Li and Na-ion system, respectively, based on constant current measurements at a C-rate of 5C.

Zhou et al. (Zhou et al., 2019) investigated the mechanism of Li

adsorption on a nanocomposite anode (G/Si) system using density functional theory. A theoretical capacity of 2896 $mAhg^{-1}$ was obtained and it was closed to the first cycle capacity of 2634 $mAhg^{-1}$ in experiment. A reversible capacity of 2383 $mAhg^{-1}$ was obtained by excluding the Li atoms with shorter bond lengths, and is comparable to the reversible capacity of 2497 $mAhg^{-1}$ in experiment. The proposed computational frame can be used to evaluate and design nanocomposite anode materials for lithium-ion batteries.

Kumar et al. (Kumar et al., 2019) developed a 2D GO sheet enveloping 1D LiMn2O4 as nanocomposite. The nanocomposite 3D porous cathode exhibits a high specific charge capacity of 130 mAh g^{-1} at 0.05 C rate and Coulombic efficiency of ~98% after 100 cycles in the potential window of 3.5–4.3 V vs Li/Li^+ with promising initial charge capacity retention of ~87%, and outstanding structural stability even after 100 cycles, giving rise to a promising cathode nanocomposite.

Huang et al. (Huang et al., 2019) explored Graphene quantum dots (GQDs) in recent years for electrochemical applications with considerable potentials. They fabricated GQD-doped $CuCo_2S_4$ nanocomposites through two-step hydrothermal process for supercapacitor electrodes. The surface of $CuCo_2S_4$ nanosheets changes from smooth to particles accumulative shape, which assists the electrochemical cycling processes as well as the ion diffusion and charge transfer kinetics for improved supercapacitor performances. GQD/$CuCo_2S_4$ electrodes demonstrated a specific capacitance of 1725 F/g under a current density of 0.5 A g^{-1} and a cycling life of 10,000 cycles by retaining 90% of the energy storage capability.

Zhang et al. (Zhang et al., 2018) reported graphene nanoscrolls bridged by crumpled graphene nanosheets as an effective conductive framework for confining SnS_2 nanosheets for lithium-ion battery (LIB) applications. The fabricated SnS_2/GNA nanocomposite is highly porous with a large specific surface area of 127.1 $m^2 g^{-1}$ and multi-scale pore structure, which can effectively prevent SnS_2 aggregation to provide abundant lithiation/delithiation sites, and buffer volumetric change and pulverization of SnS_2 nanosheets. SnS_2/GNA nanocomposite exhibits enhanced electrochemical performance with a high initial reversible capacity (1514.8 mAh g^{-1} at 0.1 A g^{-1}), excellent rate capacity (665.4 mAh g1 at 5 A g1) and good cyclic stability (1050 mAh g-1 at the 50th cycle).

Xiao et al. (Xiao et al., 2018) successfully prepared V_2O_3/rGO) nanocomposites through a facile solvothermal method and annealing process. In this synthesis protocol, V_2O_3 nanoparticles (NPs) were encapsulated by rGO. The Li^+ storage behaviour of V_2O_3/rGO was investigated in the potential range 0.01–3.0 V. The V_2O_3/rGO nanocomposite can achieve a high reversible specific capacity of 823.4 mAh g^{-1} under the current density of 0.1 A g^{-1}, and 407.3 mAh g^{-1} under the high current density of 4.0 A g^{-1}.

Wang et al. (Wang et al., 2018) developed a scalable method combining stirring-evaporation and post thermal annealing to synthesize a 3D sandwich-shaped graphene-based nanocomposite intercalated with double-shelled hollow MnCo2O4 spheres (MCO-27.2G) as anode materials for high-performance lithium-ion batteries (LIBs). The as-prepared 3D sandwich-shaped MCO-27.2G nanocomposite exhibits significantly enhanced rate capability (538 mAh g^{-1} at a high current density of 1000 mA g^{-1}) and outstanding cycle performance with high capability (703 mAh g^{-1} after 100 cycles at 200 mA g^{-1}).

Naresh et al. (Naresh et al., 2018) prepared SnO_2/rGO nanocomposite by microwave assisted hydrothermal method. The electrochemical measurements of lithium-ion batteries fabricated using pure spherical shape SnO_2 nanoparticles and crumpled nanosheets like morphology of SnO_2/rGO nanocomposite as an anode material showed the good initial discharge–charge capacity of 2128 and 1718 mA h g^{-1} respectively. The capacity retention after 50 cycles was found to be 349 mAh g^{-1} at a current density of 500 mA g^{-1} for the lithium-ion battery fabricated using pure spherical shape SnO_2 nanoparticles and the capacity retention after 300 cycles was found to be 318 mAh g^{-1} at a current density of 500 mA g^{-1} for the lithium-ion battery fabricated using SnO_2/rGO nanocomposite, which is much better than the reported values.

Lu et al. (Lu et al., 2018) fabricated a sandwich-structured SnS_2@reduced graphene oxide (SnS_2@rGO) nanocomposite consisting of SnS_2 sheets uniformly anchored on both sides of rGO sheets. The SnS_2@rGO nanocomposites, prepared through a dipping process combining with a hydrothermal method, show good electrochemical performance, including the high reversible capability of 959.2 mAh g^{-1} at 500 mA g^{-1} over 500 cycles, and superior rate performance. A full cell consisting of a commercial $LiCoO_2$ cathode and the SnS2@rGO anode delivers the stable capacity of ~821.3 mA h g^{-1} (anode basis) after 200 cycles at 100 mA g^{-1}.

Liao and Wu, (2019) adopted a facile, scalable route to synthesize egg-like few-layered graphene-wrapped and Fe_3O_4-pillared SiOx anodes (SiOx@Fe_3O_4@FLG) for lithium-ion batteries. SiOx@Fe_3O_4@FLG composites has the following attributes 833.4 mAh g^{-1} (1550 mAh cm^{-3}) at 0.5 A g^{-1} after 500 cycles with 81.8% capacity retention ratio which makes SiOx@Fe_3O_4@FLG composites promising anode materials for high-energy Li-ion battery.

Li et al. (Li et al., 2018) designed and fabricated a novel MoS_2@SnO_2–SnS_2 composite via a two-step simple hydrothermal route. Due to the synergistic effect between the ultrathin MoS_2 nanosheets and the SnO2–SnS_2 nanosheets, the MoS_2@SnO_2–SnS_2 composite exhibits excellent electrochemical performance as anode for LIBs.

Kumar et al.(Kumar et al., 2018) synthesised LFS/CNF(5 wt%)/rGO (5 wt%) nanocomposites using solvothermal method followed by annealing at 600 °C for 4 h under continuous flow of argon., LFS/CNF/rGO shows a higher surface area of 88m^2/g compared to 62m^2/g for LFS/CNF. Correspondingly, the glavanostatic charge–discharge curves show an improved discharge capacity of 260 mAh·g^{-1} and 135 mAh·g^{-1} at C/20 and 8 C rates for LFS/CNF/rGO, compared to 230 mAh·g^{-1} and 116 mAh·g^{-1} at the same rates for LFS/CNF. This is further corroborated by the analysis of electrochemical impedance spectroscopy (EIS) data using a modified Randles circuit showing a factor of two increase in Li-ion diffusion coefficient (4.2×10^{-13} cm^2/s) and higher exchange current density in LFS/CNF/rGO nanocomposite.

Hu et al. (Hu et al., 2019) synthesised (DS-Co_3Sn_2/SnO_2@C@GN) via a series of combined procedures containing co-precipitation, hydrothermal reaction for carbon coating, stirring for mixing and calcination. It used as the anode electrode of LIBs, it exhibits the superior performance with a reversible charge storage capacity of 744 mA g^{-1} after 100 cycles and 605 mA g^{-1} after 300 cycles at a current density of 0.1 A g^{-1}. DS-Co_3Sn_2/SnO_2@C@GN micro-cube also shows good sodium storage capacity.

3.2. Supercapacitor

Ultracapacitors based on electrochemical double layer capacitance (EDLC) are electrical energy storage devices that store and release energy by nanoscopic charge separation at the electrochemical interface between an electrode and an electrolyte. GO and rGO have been used in capacitors and they are attractive because of their high specific surface area, low electrical resistance, low mass density, and high cyclic stability.

In recent years, several research groups have produced and explored the use of graphene nanocomposite supercapersitor:

Ates et al. (Ates et al., 2018) synthesised rGO and rGO/Zn nanoparticle/polycarbazole (rGO/Zn/PCz) nanocomposite by in situ chemical reactions. Nanocomposites were examined by scanning electron microscopy-energy-dispersive X-ray analysis (SEM-EDX) and Fourier-transform infrared spectroscopy-attenuated transmission reflectance (FTIR-ATR). Electrochemical measurements of supercapacitors were tested by galvanostatic charge-discharge (GCD), CV, and EIS. rGO/Zn/PCz nanocomposite showed increased capacitance (Csp = 33.88 F/g) compared to that of rGO (Csp = 20.78 F/g), PCz (12.57 F/g), and Zn/

PCz (19.05 F/g) at the scan rate of 10 mV/s by CV method. The enhanced capacitance results in high-power (P = 442.5Wkg^{-1}) and energy-storage (E = 1.66 Wh kg^{-1}) capabilities of the rGO/Zn/PCz nanocomposite material. Stability tests were examined for 1000 cycles by CV method.

Chien et al. (Chien et al., 2018) synthesised rGO-carbon black (CB) and CB nanocomposite coated carbon cloth electrodes. They use a nitrogen DC-pulse atmospheric pressure plasma jet (APPJ) to process the electrodes. The APPJ processing time was < 40 s. Replacing part of the CB with rGO nano-flakes can increase the overall surface area to improve the supercapacitive performance. Specifically, by replacing 50 wt % of CBs with rGOs, the specific (areal) capacitance can be improved from 91.84 F g^{-1} (19.74 mF/cm^2) to 162.68 F g^{-1} (29.16 mF/cm^2), respectively, with 20 s APPJ processing time, as evaluated by cyclic voltammetry under a potential scan rate of 2 mV s^{-1}.

Bao et al. (Bao et al., 2018) synthesised a polyaniline/sulfonated graphene (PANI/SG) nanostructure as electrode material for an asymmetric supercapacitor via a novel in situ chemical oxidative polymerisation method including two oxidants. The composite's structure and morphology were characterized by FTIR, XRD, XPS, field-emission scanning electron microscopy (FESEM), and TEM measurements. The electrochemical performances of the composite were characterized by CV, galvanostatic charge–discharge (GCD), and EIS techniques in detail. They manufactured an asymmetric supercapacitor (ASC) employing activated carbon (AC) and PANI/SG as the positive and negative electrodes, respectively. The ASC possessed an extended potential window (1.4 V), a remarkable cycling property (85.9% capacitance retention after 5000 cycles), and a satisfactory average energy and power density (23 Wh/kg and 6.1 kW/kg).

Guirri et al. (Giuri et al., 2018) developed a green ternary nanocomposite based on PEDOT:PSS doped with GO and glucose (GGO-PEDOT) with a specific capacitance of 16 F/g, indicating how this nanocomposite is potentially suitable to be used as an electrode material for a supercapacitor. Analyses, such as thermogravimetric, colorimetric and contact angle measurements, were performed aiming at assessing the stability of the thermal and of the surface properties, even in severe moisture and UV aging conditions.

Jayachandrian et al. (Jayachandiran et al., 2018) synthesized ZnO and rGO/ZnO nanocomposite as an electrode material for supercapacitor application. A simple and cost effective method called ultrasonic-assisted solution process was used to synthesis rGO/ZnO nanocomposite. The prepared ZnO and rGO/ZnO nanocomposite were characterized by XRD, FESEM, TEM and confocal Raman. The electrochemical studies of rGO/ZnO nanocomposite exhibited that the composite has the higher specific capacitance (312 F/g) compared to pure ZnO (200 F/g) with better cycling stability up to 1000 cycles.

Lin et al. (Lin et al., 2018) synthesized CoNi2S4/graphene nanocomposites by a simple solvothermal method and used as supercapacitor electrodes. Electrochemical performance of CoNi2S4/graphene nanocomposite electrodes showed that it possessed pseudocapacitive behaviour with high specific capacitance (1621 F/g at 0.5 A g^{-1}), good rate capability (76.7% capacitance retention when reaching 10 A g^{-1}) and outstanding cycling stability (no capacitance loss after 2500 charge–discharge cycles at 5Ag^{-1}).The material also shows a high specific capacitance of 126.6 F g^{-1} at 0.5 A g^{-1}, good cycle stability with capacitance retention of 87.4% after 5000 cycles and the highest energy density of 39.56 W h kg^{-1} at the power density of 374.8 W kg^{-1}.

Low et al. (Low et al., 2018) synthesised graphene/$Ni_3V_2O_8$ nanocomposites by a facile solvothermal approach in which the graphene sheets were fabricated via the environmentally benign liquid phase exfoliation with optimised ethanol to water volume ratio (2:3). The nanocomposites integrated separately the advantages of graphene sheet and pseudocapacitive nature of $Ni_3V_2O_8$ and hence possessed electrochemical performance which outperformed the pristine Ni3V2O8. G-4NVO (graphene/$Ni_3V_2O_8$ with the weight ratio of 1:4) nanocomposite proved to be a promising electrode material, as it delivered eminent specific capacitance of 748 Fg1 at current density of 0.5 Ag-1, remarkable energy density of 103.94 Wh/kg at power density of 45.61 kW/kg, reasonable cycling stability with 71% capacitance retention and superior coulombic efficiency of 83% after 3000 charge-discharge cycles at 0.5 Ag^{-1}.

Amity et al. (Maity et al., 2018) fabricated Flower like ZnO and plate like CuO upon rGO and Nitrogen doped rGO following a simple scalable cheapest facile hydrothermal treatment. XRD, FTIR and XPS analysis confirm the Formation of N-doping on rGO as well as all composites. They derived a superior energy density (ED) value of the fabricated nanocomposite to be 95.55Whkg^{-1} with power density (PD) 399.97 Wkg^{-1}. The electrode made up of hybrid ZnO–CuO/N-rGO nanocomposites displays excellent cyclic stability of 88% retention of specific capacitance after completion of 5000 cycles.

Nagarani et al. (Nagarani et al., 2018) synthesised SnO_2/Co_3O_4 (BTMO) with rGO nanocomposite by co-precipitation method to determine its electrochemical properties for the betterment of Supercapacitor applications. The composite was characterised with XRD and SEM. BTMO/rGO nanocomposite has alteration in surface to volume ratio and improved electron conductivity were observed with increased integral area and current such as 2.5117×10^{-4} A/s and 3.1686×10^{-4} A respectively in CV behaviour. BTMO/rGO nanocomposite also has an increased specific capacitance value of 317.2 F/g at 1 A/g. The increased specific capacitance value of BTMO/rGO nanocomposites are mainly due to the synergistic effect between SnO_2/Co_3O_4 and rGO.

Ndiaje et al. (Ndiaye et al., 2018) studied the electrochemical performance of hydrothermal synthesized three dimensional (3D) orthorhombic vanadium pentoxide (V_2O_5) nanosheets and vanadium pentoxide/graphene foam (V_2O_5/GF) composites at different mass loading of GF. The hybrid device of V_2O_5/GF-150 mg//C–Fe/PANI demonstrated a high energy density of 39 Wh kg^{-1} with a corresponding high power density of 947 W kg1 at a specific current of 1 A g^{-1} in an operating voltage window of 0.0–1.6 V. The hybrid device also exhibited an excellent cycling stability with 74% capacity retention recorded for up to 10,000 constant charging–discharge cycles and an excellent ageing test at a specific current of 10 A g^{-}1. Fig. 4.

Pu et al. (Pu et al., 2018) demonstrated a facile hydrothermal method for synthesizing N-doped graphene/Fe_2O_3 nanocomposite and its application to supercapacitors. Samples prepared with and without N-doping were characterized and their electrochemical performances compared. N-doping increased the specific capacitance at 1 A/g from 543 F/g to 698 F/g. A capacitance as high as 354 F/g was retained when the current density was raised to 20 A/g.

Singu et al. (Singu and Yoon, 2019) produced exfoliated rGO manganese oxide nanocomposites (rGO-MnOx and rGO-Mn_3O_4) and systematically analysed by spectral, thermal, elemental and electron microscope. The rGO-MnOx nanocomposite exhibiting the utmost capacitance of 398.8 F/g at a sweep rate of 5 mV/s, the energy density of 23.3 Wh kg^{-1} and power density of 2001 W/kg, owing to the synergistic effect of reduced graphene oxide and spherical and cubical shape of manganese oxide nanoparticles Fig. 5.

Huang et al. (Huang et al., 2019) presented GQD-doped $CuCo_2S_4$ nanocomposites through two-step hydrothermal process for supercapacitor electrodes. GQD/$CuCo_2S_4$ electrodes demonstrated a specific capacitance of 1725 F/g under a current density of 0.5 A g^{-1} and a cycling life of 10,000 cycles by retaining 90% of the energy storage capability. As such, this work extends the potential of GQDs in electrochemical applications by means of morphology change of $CuCo_2S_4$ nanosheets.

Xing et al. (Xing et al., 2018) prepared three-dimensional (3D) flower-shaped $Li_4Ti_5O_{12}$-graphene (Gr) hybrid micro/nanostructures and pine needles derived carbon nanopores (PNDCN) by using the effective hydrothermal process. 3D $Li_4Ti_5O_{12}$-Gr displayed a high specific capacitance of 706.52 F/g at 1 A g^{-1}. The prepared PNDCN also

exhibits high specific capacitance of 314.50 F/g at 1 A g^{-1} benefiting from its interconnected honeycomb-like hierarchical and open structure, which facilitates the diffusion and reaction of electrolyte ions and enables an isotropic charging/discharging process. An asymmetric supercapacitor utilizing $Li_4Ti_5O_{12}$-Gr as positive electrode and PNDCN as negative electrode has been fabricated, it delivers a high energy density of 35.06 Wh kg^{-1} at power density of 800.08 W/kg and outstanding cycling stability with 90.18% capacitance retention after 2000 cycles.

Tabrizi et al. (Tabrizi et al., 2018) fabricated asymmetric supercapacitor (ASC), using nanoarrays of polyaniline grown on graphene oxide sheets (PANI-GO) as positive electrode and also, carbonized nitrogen-doped carbon nanoarrays grown on the surface of graphene (CPANI-G) as negative electrode. The fabricated PANI-GO//CPANI-G ASC exhibited a remarkably enhanced maximum energy density of 52 Wh kg^{-1}. Furthermore, ASC electrode exhibits excellent cycling durability, with 90.3% specific capacitance.

Sunduriya et al. (Sundriyal et al., 2018) reported the synthesis of a composite of TiO_2 nanosheets (NS) with rGO for supercapacitor applications. The rGO/TiO_2 NS composite was used to fabricate a flexible electrode which, in presence of 1 M H_2SO_4 as an electrolyte, has shown a high specific capacitance of 233.67 F/g at a current density of 1 A/g within a potential window of 0–1 V. The fabricated composite electrode has displayed a long-term cyclic stability, retaining a specific capacitance of 98.2% even after 2000 charge–discharge cycles. The rGO/TiO_2 NS electrode has delivered high values of energy (32.454 Wh/kg) and power (716.779 W/kg) densities. Interestingly, it is possible to retrieve a sufficiently high energy density of 24.576 Wh/kg which could generate a power density value of as high as 2142.84 W/kg.

Sephra et al. (Sephra et al., 2018) synthesised SnO_2 nanospheres rGO) composite. Hybrid nanocomposite in 1:3 ratio exhibited (i) excellent methylene blue degradation capability within 3 min under visible light condition and (ii) high specific capacitance of 337.52 F/g at 0.5 A/g in 1 M H_2SO_4 electrolyte with 89% of retention after 5000 cycles.

3.3. Biosensor

Graphene combined with polymer improves the performance of biosensors as far as selectivity, sensitivity, and response time, of biosensors for clinical diagnostics, metal ion speciation, formations of batteries and capacitors. In recent years, several research groups fabricated graphene nanocomposite for biosensor applications Table 2:

3.3.1. Electrochemical biosensors

Gupta et al. (Gupta and Meek, 2018) developed metal nanoparticles–grafted functionalized graphene nanosheets with nanostructured polyaniline (PANi) 'hybrid' nanocomposites for ascorbic acid (AA) sensing. The versatility of the nanocomposite performance was corroborated by altering size and density of electrodeposited gold (AuNP) and silver (AgNP) nanoparticles on the graphene oxide; GO, thermally reduced GO; rGO and nitrogenated functionalized graphene; NFG. The multilayers (PANi|AgNP|GFN and PANi|AuNP|GFN) on fluoride-doped tin oxide (FTO) coated glass, graphite foil (GF) and graphene rod (GR) electrodes were tested that show increased electrical conductivity and reduced charge transfer resistance. They demonstrated ultrasensitive detection of AA analyte over full range (from 1×10^{-12} M to10×10^{-3} M) with linear sensitivity 10 mA mM^{-1} cm^{-2} and excellent limit of detection < 1 pM having high signal-to-noise ratio following PANi|AuNP|NFG ≤ PANi|AgNP|NFG < AuNP|NFG < AgNP|NFG.

Hatmluyi et al. (Hatamluyi and Es'haghi 2018) used PAMAM dendrimer/reduced graphene oxide nanocomposite modified pencil graphite electrode (PAMAM/rGO/PGE) to fabricate an electrochemical DNA biosensor for determination of Rituxan (RTX) at low concentrations. The fabricated biosensor was characterized with FE-SEM, EIS, and CV techniques and when experimental conditions were optimised, a wide linear relationship between RTX concentration and guanine signal was obtained within the range of 7.0–60.0 mmolL1 and 60.0-to 300.0 mmolL1 detection limit (0.56 mmol L^{-1}). The reproducibility, stability, and performance of the constructed biosensor was examined by quantitative measuring RTX in pharmaceutical and human serum samples with good precision (RSD; 2.0–6.0%) and acceptable recoveries (100.04–101.95%).

Huang et al. (Huang et al., 2018) prepared a novel non-enzymatic sensor based on reduction graphene oxide-persimmon tannin-platinum nanocomposite (rGO-PT-Pt) for H_2O_2 detection. rGO-PT-Pt nanocomposite was characterized by SEM, TEM, UV–vis) and FT-IR. Under the optimal conditions, the rGO-PT-Pt non-enzymatic biosensor exhibited outstanding electrocatalytic activity towards H_2O_2 reduction. The amperometric response demonstrated a linear relationship with H_2O_2 concentration from 1.0 to 100 μM with the correlation coefficient of 0.9931. The limit of detection was 0.26 μM (S/N = 3) and the response time was 3 s.

Mathew et al. (Mathew et al., 2018) fabricated magnetic hematite (α-Fe_2O_3) decorated electrochemically reduced graphene oxide (α-Fe_2O_3@erGO) nanocomposite. The composite was characterised by XPS and Rahman spectroscopy and when used as sensor, it exhibited linear dynamic ranges over 0.25–100 μM in response to DA with a LOD of 0.024 μM (S/N = 3), LOQ of 0.08 μM (S/N = 10), and a sensitivity of 12.56 μAμM^{-1} cm^{-2}.

Shoja et al. (Shoja et al., 2018) fabricated a composite based on two-step electropolymerization of Ni(II)-oxytetracycline conducting metallopolymer nanoparticles (Ni-OTC NPs) on the surface of pencil graphite electrode (PGE) which was modified by reduced graphene oxide/carboxyl functionalized ordered mesoporous carbon (rGO/f-OMC). The composite used as biosensor was characterized by field emission scanning electron microscopy (FE-SEM), XRD, FT-IR spectroscopy, EDX, CV and Nitrogen adsorption–desorption analysis. Under optimal conditions, the prepared biosensor showed long-term stability (21 days) with a wide linear range from 0.1 μM to 3 μM with high sensitivity (0.0188 mA/μM) and low detection limit (120 nM).

Sukrobov et al. (Sukhrobov et al., 2018) described production of

Table 2
Biosensors based on Graphene nanocomposites.

Materials	Analyte	References
rGO-ZnO	DNA & TNT	(Hatamluyi and Es'haghi, 2018)
G-CdS-DNA	Catechol	
G-NiO	Cholesterol	(Proa-Coronado et al., 2018)
G-AuNPs	DNA	(Hatamluyi and Es'haghi, 2018)
rGO- AuNP	H_2O_2	(Huang, Y. et al., 2018)
rGO-PLL-MnO2	Glucose oxidase, H_2O_2	(Sukhrobov et al., 2018)
rGO-PLL-Mn3O4	Glucose	Xue et al. (2018)
rGO-AuNPs non-enzymatic	H_2O_2	(Huang, Y. et al., 2018)
rGO-AuNPs- non-enzymatic	H_2O_2	(Huang, Y. et al., 2018)
Aminophenylboronic acid (APBA)-functionalized rGO	Glucose, glycated hemoglobin	Xue et al. (2018)

composite of nickel nanoparticles (NiNPs) decorated on Nafion-graphene composite film by using the electrochemical deposition method which was used to fabricate electrochemical biosensors for sensitive nonenzymatic glucose detection. The NiNPs/Nafion/graphene/GCE at an applied potential of +0.55 V in a linear range of 1–200 μM presented a high sensitivity of 3437.25 μA $mM^{-1}cm^{-2}$ with coefficient of correlation R2 = 0.999; and in a linear range of 200–10800 μM it performed the best sensitivity of 2848.6 μA $mM^{-1}cm^{-2}$ with coefficient of correlation R2 = 0.995 towards glucose oxidation. For a concentration up to 200 μM, a linear range was obtained with a limit of detection of 0.6 μM (signal to noise = 3) and as much as 10800 μM with a limit of detection of 0.82 μM (signal to noise = 3). The time of responses was about 1–1.5s with the addition of 0.1–1 mM glucose. The NiNPs/Nafion/graphene/GCE exhibited high sensitivity, low working potential, good stability, excellent electrical properties, enhanced selectivity and fast amperometric responses to glucose oxidation.

Xue et al. (Xue et al., 2018) fabricated a novel non-enzymatic glucose sensor based on the reduction graphene oxide-persimmon tannin-platinum-palladium alloy (rGO-PT-Pt-Pd) nanocomposite. The rGO-PT-Pt-Pd nanocomposite was prepared through a facile approach with PT as film material and ascorbic acid as reducing agent and characterized by UV–vis, FT-IR, SEM and XRD. rGO-PT-Pt-Pd nanocomposite was employed as an electrode material for non-enzymatic glucose sensing using gold electrode (GE). The sensor exhibited a wide linear range of 0.01–0.40 mol/L with a limit of detection (1.43 μmol/L) as well as high stability and fast responsetime (< 3s).

Zhang et al. (Zhang et al., 2018) explored a novel dopamine biosensor based on carbon fiber microelectrodes (CFMEs) modified with copper(I) sulphide functionalized nanocomposites of the reduced graphene oxide (Cu_{2+}S/rGO) for the sensitive detection of dopamine and in vivo monitoring the neurotransmitters released by Drosophila's brain. The Cu^{2+}S/rGO decorated microelectrodes were characterized by SEM and XPS, and CV. Their observations demonstrated that Cu_{2+}S/rGO-CFMEs exhibited excellent catalytic activity and high selectivity for dopamine with relatively low detection limit (24 nM), wide linear range (i.e., from 0.1 to 20 βM) and outstanding reproducibility.

3.3.2. Field effect transistor (FET) biosensor

Proa et al. (Proa-Coronado et al., 2018) prepared a multilayered reduced graphene oxide decorated homogenously with Platinum nanoparticles (rGO/Pt).The composite was characterised by XRD, TEM, XPS and CV. The nanocomposite was used as a transducer in Back-gated Field Effect Transistor (GFET) based nanobiosensors. The CS2, rGO/Pt and protein G that detects IgG, were locally deposited by using a commercial microplotter instrument.

Chen et al. (Chen et al., 2017) developed a reduced graphene oxide-based field-effect transistor method for real-time detection of the Ebola virus antigen. This method uses the attractive semiconductor characteristics of graphene-based material, and instantaneously yields highly sensitive and specific detection of Ebola glycoprotein. The feasibility of this method for clinical application in point-of-care technology is evaluated using Ebola glycoprotein suspended in diluted PBS buffer, human serum, and plasma. These results demonstrate the successful fabrication of a promising field-effect transistor biosensor for EVD diagnosis.

3.3.3. Optical biosensor

Optical biosensors have recently been used to detect different biological molecules, such as cancer biomarkers (Wu et al., 2019), glucose, H_2O_2, dopamine, NAs, food toxins and metal ions, which are of great interest to medicine (Cheng et al., 2019).

Fluorescence-based detection has become an attractive research area for a wide range of applications. It is used for Nucleic acid sensors where the target-triggered conformational change of an oligonucleotide affects the fluorescence of DNA-binding dyes such as OliGreen, TOTO, and ethidium bromide (Du and Dong, 2017).

Li et al. (Li et al., 2016) developed tyramine (TYR)-functionalized GQDs (TYR-GQDs) for fluorescent biosensing of H_2O_2 and four metabolites including glucose, cholesterol, L-lactate, and xanthine in the blood. In the TYR-GQDs conjugate, the tyramine is covalently attached on the surface of GQDs through the reaction between the amino (–NH_2) groups of TYR and carboxyl (–COOH) groups of GQDs. In order to detect these four metabolites, their corresponding oxidases such as glucose oxidase, cholesterol oxidase, L-lactate oxidase, and xanthine oxidase were added into the 10 mM PBS (pH 7.0) containing 0.1 mg mL^{-1} TYR-GQDs conjugate to trigger photoluminescence (PL) quenching.

Chen et al. (Chen et al., 2011) demonstrated a GO-based label-free near infrared (NIR) fluorescent sensor for detecting dopamine. The good affinity of DA molecules with GO allows multiple noncovalent interactions. The effective quenching of GO when DA molecules are adsorbed onto the GO nanosheet enables biosensing by way of direct readout of the NIR fluorescence of the GO in the NIR for the effective detection of DA. The sensor showed an LOD of 94 nM and a 2.0% relative standard deviation; it was used to DA determination in biological fluids with 98–115% quantitative recovery.

Liu et al. (Liu et al., 2013) developed a fluorescent DNA sensor and aptasensor for the detection of infectious pathogens based on a silver nanocluster/GO hybrid system. By conjugating oligonucleotide sequences to NA-protected AgNCs, the fluorescence was generated by the desorption of AgNCs from GO surface by forming duplex DNA structures or complexes with aptamer-substrate. This approach enabled thrombin detection with an LOD of 0.5 nM. The hybrid biosensor was also used for the detection of HBV, HIV, and *Treponema pallidum* (syphilis) genes.

3.4. Solar cell

Energy devices such as solar cells, fuel cells and supercapacitors have been used in numerous low-cost and novel nano-structured materials. In recent years, several research groups have investigated the production and the use graphene nanocomposite in solar cell;

Aydin (Aydın, 2019) investigated rGO based nanocomposites produced via microwave hydrothermal method and their variation with SnO_2 at different atomic ratios (10, 20, 30 and 40%). The composite was characterised using XRD, DTA, TGA, FTIR, dielectric measurements, SEM, TEM and UV spectroscopy. The adding of SnO2 at various amounts affects the dielectric, optical and thermal properties of the rGO, as well as the ac and dc conductivity. The crystallite sizes of the as-prepared samples are in the range of 3.42e3.70 nm. The addition of SnO2 cause the significant changes in the value of the activation energy. The characteristic peak of the rGO is shifted from 253 to 268 nm by increasing amount of SnO2. The effects of SnO_2 content on the thermal stability investigated from room temperature to 700 C, was detected.

Gao et al. (Gao et al., 2019) investigated the feasibility of the hybrid nanocomposites of the graphene quantum dot (GQD) and the phenoxazine-based dyes as the efficient sensitizer of the dye-sensitized solar cell (DSSC). Based on the first principles density functional theory (DFT), the geometrical structures of the separate GQDs, the phenoxazine-based dyes, and their hybridized nanocomposites are fully optimized. The energy stabilities of the obtained structures are confirmed by harmonic frequency analysis. The optical absorptions of the optimized structures are calculated with the time-dependent DFT (TDDFT).

Chauhan et al.(Chauhan et al., 2019) reported a new method for the synthesis of zinc oxide (ZnO) nanoflowers/GO composite, uniformly grown over Silicon (Si) substrate. The nanocomposite (GO/ZnO) was fabricated by mixing of GO and ZnO nanoseed solution followed by vigorous ultra-sonication and spin-coating over the Si substrate. The nanocomposite was characterised by various techniques such as Field emission scanning electron microscopy (FESEM), FTIR, Raman spectroscopy and XRD analysis. The performance of nanocomposite was analysed for remediation of methylene blue (MB) dye by utilizing

sunlight as an energy source to initiate the photoreaction. The composite (GO/ZnO) shows ~33% faster decolourisation of 20 mg/L of MB dye in comparison with pure ZnO.

Zhao et al. (Zhou et al., 2018) synthesised a multiple transmission channels, heterojunction and 3D PCN/AgBr/rGO photocatalyst by introducing the rGO covering AgBr onto the surface of 3D porous g-C3N4 (PCN). The 3D PCN/AgBr/rGO nanocomposite exhibited excellent photocatalytic efficiencies for tetracycline (TC) up to 78.4% within 90 min and 2,4-dichlorophenol (2,4-DCP) up to 68.2% within 6 h. The photocatalytic rate of PCN/AgBr/rGO was much higher than 3D PCN (21%), AgBr particles (31%) and most of g-C3N4-based photocatalysts in TC degradation.

Timoumi et al. (Timoumi et al., 2018) prepared TiO_2-Graphene Oxide (TiO_2-GO) nanocomposite thin films of different grades using Titanium Tetra Isopropoxide (TIP) and GO nanosheet suspensions coated on a glass plate by a spin coating technique. TiO_2-GO nanocomposite film samples were thoroughly characterized for their morphology, thickness and band gap changes by coating a thin layer of 250 nm thickness on a 2 cm × 2 cm glass plate. The analysis of optical absorption data showed that the values of band gap energy decreased from 3.62 eV to 1.40 eV with increasing dopant quantity. This reduction might be attributed to electron and/or hole trapping at the donor and acceptor levels in the TiO_2 band structure.

Ranjbar et al. (Ranjbar and Shahrokhian, 2018) fabricated of an effective and durable sensing platform based on gold nanoparticles/carbon nanoparticles/cellulose nanofibers nanocomposite (AuNPs/CNPs/CNFs) at the surface of glassy carbon electrode for sensitive and selective detection of *Staphylococcus aureus* (*S. aureus*). The AuNPs/CNPs/CNFs nanocomposite with the high surface area, excellent conductivity, and good biocompatibility was used for self-assembled of the thiolated specific *S. aureus* aptamer as a sensing element. The surface morphology of AuNPs/CNPs/CNFs nanocomposite was characterized with FESEM, EDS, dynamic light scattering (DLS) and UV–Vis spectrophotometric methods. Each aptasensor modification step was monitored with CV and EIS techniques. The fabricated aptasensor exhibited a wide linear dynamic range (1.2×10^1 to 1.2×10^8) CFU mL^{-1} with a LOD of 1 CFU mL^{-1}.

Ramawati et al. (Rahmawati et al., 2018) produced rGO/polyaniline nanocomposites with reduced graphene oxide (rGO) using sonication-assisted oxidation of graphite followed by reduction with ascorbic acid as reductor. The rGO and polyaniline were blended in three mass compositions of 1:3, 1:1, and 4:1 to produced rGO/polyaniline nanocomposites. The rGO/polyaniline nanocomposites were characterized using Raman spectroscopy, FTIR spectroscopy and LCR meter. The best performance was obtained for rGO/Polyaniline ratio of 4:1. With optimum short circuit current density (Jsc), the open circuit current (Voc), the fill factor (FF), and the overall conversion efficiency under AM 1.5, 100 mW cm^{-2} illumination are 7.853 mA/cm2, 0.64 V, 47.2% and 2.64%, respectively.

3.5. Corrosion

Corrosion is known as one of the most degradation processes in manufacturing industries. Therefore, reducing methods of corrosion and wear costs are being greatly investigated. Graphene is impermeable to all molecules and has high chemical stability, which makes it an excellent anticorrosion coating for metals. In USA, annual direct cost of damage due to steel corrosion in infrastructure (bridges, pipelines, storage, etc.), utilities (drinking water, gas/electric appliances, etc.), automotive industries and government defence facilities is around US $300 billion. Corrosion, which triggered by moisture, oxygen, sulphur, electrolytes, etc., is one of the greatest challenges encountered by industries and government sectors that utilize metals and their alloys (D. Dwivedi, Lepková et al., 2017). In recent years, several research groups have used graphene nanocomposite as anti-corrosion coating;

Dutta et al. (Dutta et al., 2018) reported the interactions between the filler and the polymer were found to be a key factor governing anticorrosion performance. The advantage of graphene as a filler in anticorrosion coatings lies in its dispersibility and miscibility with both the casting solvent and the polymer. Due to the insulating nature of polymers, graphene–polymer composite coatings with a strong interaction between the filler and the polymer matrix are an alternative means of addressing corrosion issue. A bilayer coating with EC-graphene additives for PU over epoxy has been found to reduce the corrosion rate (CR) to 1.81×10^{-5} mm per year. With a graphene loading of less than 1%, this represents the lowest CR ever achieved for copper and steel substrates and a diffusion coefficient that is lower by a factor of nearly 2.2 than that of the pristine polymer.

Taheri et al. (Taheri et al., 2018) modified the negatively charged GO nanosheets with polyaniline (PAni) nanofibers and zinc cations through a layer-by-layer assembly method. The structure, morphology and thermal behavior of GO, GO-PAni and GO-PAni-Zn were characterized using EIS and polarization tests. The results confirmed high cation exchange capability and better anti-corrosion properties of GO-PAni-Zn sample than others. The theoretical outcomes derived from quantum mechanics computations revealed that inorganic zinc cations demonstrated electrostatic and cation-p interactions with emeraldine.

Yasin et al. (Yasin et al., 2018) fabricated Nickel–graphene nanocomposite coatings onto the mild steel by electrochemical co-deposition technique. Their research demonstrated the properties of nickel–graphene composite coatings influenced by different electrodeposition current densities. The improved mechanical properties and superior anticorrosion performance of composite coatings are obtained at the peak value of current density of 9 Adm^2.

Jiang et al. (Jiang et al., 2019) GO to polypyrrole (PPY) matrix, furthermore, PPY-GO composite coatings with different GO content were insitu electrodeposited on 304 stainless steel (SS) bipolar plates to protect them from corrosion in the aggressive working environment. The PPY-GO coating with the optimized GO content of 1 $mgmL^{-1}$ in the electrodeposition electrolyte shows the best corrosion resistance among the prepared coatings.

Xu et al. (Xu et al., 2019) constructed superior corrosion-resistant magnetic graphene foams decorated by Fe_3O_4 (MGF@Fe_3O_4) through in-situ simultaneous deposition of ferrous ion (Fe^{2+}) induced GO. The composites were characterised using Raman spectroscopy, X-ray, XPS, XRD, SEM, TEM, vibrating sample magnetometer (VSM) and vector network analyser. These 3D porous MGF@Fe_3O_4 exhibit much better electromagnetic wave (EMW) absorption properties and corrosion resistance than 2D hybrid materials of magnetic metal particles and graphene sheets. Their minimum reflection loss (RLmin) value reaches −64.4 dB at 10.8 GHz and maximum effective absorption bandwidth (EAB) is up to 6.0 GHz from 12 GHz to 18 GHz with a matching thickness of 2.4 mm. After treatment in hydrochloric acid for 70 days, the acid-treated MGF@Fe_3O_4 still keeps excellent EMW absorption performance with their decrease of saturation magnetization lower than 16%.

Xue et al. (Xue et al., 2019) fabricated graphene oxide-hydroxyapatite (GO-HAP) nanocomposite with stable structure via in-situ bonding technology. The GO-HAP nanocomposite, as an anticorrosion pigment, exhibits a remarkable anticorrosion performance. In comparison with blank epoxy resin system, the impedance value of 0.6% GO-HAP/epoxy increases by 754.4%.

3.6. Membrane

Graphene oxide composite is a promising material that has attracted numerous researchers in order to improve membrane properties and separation performance Fig. 9. In recent years, several research groups have used graphene nanocomposite as membranes:

Kim et al. (Kim et al., 2018) fabricated GO-polymer composite without covalent bonding between GO and polymer, leading to a combination of mechanical robustness, remarkable water transport properties, and an anti-swelling tendency suitable for the high-pressure

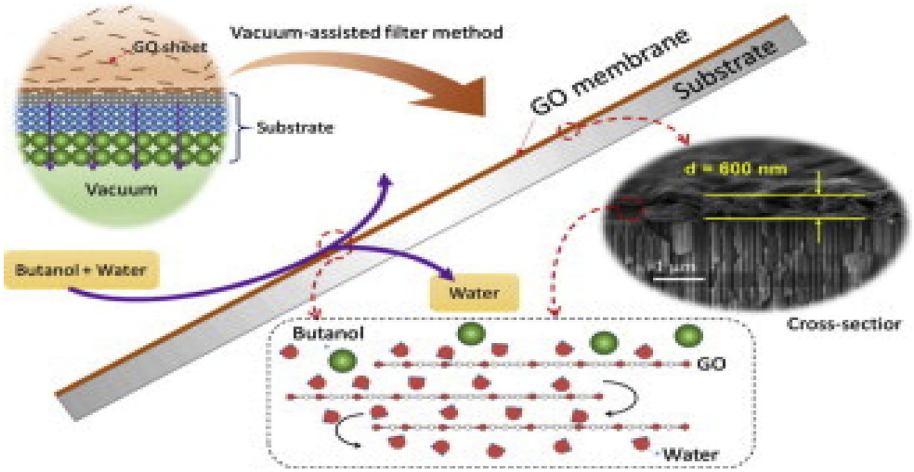

Fig. 9. A typical GO composite membrane.

operation required for reverse osmosis (RO) membrane process. The resulting GO-polymer membrane was not swollen during RO operation while it was stable under a harsh oxidising environment. It also demonstrated water flux of 33.5 $Lm^{-2}h^{-1}$ with 98.5% NaCl rejection at 10 bar when prepared by high-vacuum filtration and subsequent polymerisation of the precursor solution on to a mesoporous substrate.

Kausar, (2018) fabricated PMMA-co-MA-PEG/PC and GNR-based nanocomposite. Tensile strength and Young's Modulus of PMMA-co-MA-PEG/PC/GNR0.5–3 increased from 64.3 to 74.7 MPa and 76.7–99.9 MPa, respectively. GNR loading increased the permselectivity aCO2/N2 (25.4–41.6) of nanocomposite membrane relative to blend membrane (20.1). However, permeability PCO_2 was decreased from 163.9 to 139.7 Barrer than blend (174.3 Barrer). PMMA-co-MA-PEG/PC/GNR revealed 51.6% increase and 24.7% decrease in permselectivity and permeability owing to molecular sieving and barricade characteristics of graphene nanoribbon.

Swain et al. (Swain et al., 2018) demonstrated the development of high-performance polysulfone (PSf) hybrid mixed matrix membranes (MMMs) through the collaborative inclusion of multiwalled carbon nanotubes (CNTs) and rGO. The nanofillers were aligned by virtue of an AC electric field in order to formulate a multifunctional composite membrane structure for selective separation of O_2/N_2 gas. The inclusion of rGO nanosheets established a long, tortuous path hindering the permeation of gas molecules possessing the larger molecular size.

Zhao et al. (Zhao et al., 2018) prepared a high flux thin film nanocomposite (TFN) nanofiltration (NF) membrane under low pressure (4 bars) through a facilitated interfacial polymerization (IP) reaction between low concentrations of piperazine (PIP) and organic trimesoyl chloride (TMC) in the presence of GO nanosheets. At optimized GO dosage of 0.01 wt%, the synthesized GO-TFN membrane achieved a water permeance of 15.63 L/m^2 h bar with the Na_2SO_4 rejection of 96.56% and $MgSO_4$ rejection of 90.5%. The characterization of the TFN membranes by SEM, AFM, zeta potential and FTIR revealed that GO nanosheets improved the surface roughness, hydrophilicity and surface charges at low PIP and TMC concentrations, leading to both high water flux and salt rejection.

Jin et al. (Jin et al., 2019) synthesised PI/MP-GO nanocomposite. The MP-GO was found to be an effective base-catalysts for the thermal conversion of polyamic acid (PAA) precursor to PI. When 3 wt% of MP-GO was added to the PI matrix, the complete imidization of nanocomposites was achieved at a temperature lower than 200 °C. In addition, the PI/MP-GO nanocomposite films exhibited reinforcement of the oxygen barrier properties which were even better than those of pristine PI, due to the excellent dispersion state of MP-GO and the favourable non-covalent interaction between MP-GO and the PI matrix. Comparison to pristine PI, the oxygen permeability of nanocomposite films that contained only 1 wt% of MP-GO loading was significantly decreased, by about 80%.

3.7. Gas sensor

Sensitive and selective detection of gases at room temperature is required for proper environmental monitoring and also to avoid any health hazards in the industrial areas. In recent years, several research groups have produced and explored the use of graphene nanocomposite gas sensor:

Achary et al. (Achary et al., 2018) exploited, a low-cost, one-step and combustion route mediated rGO-$CuFe_2O_4$ nanocomposite as a high–performance NH_3 gas sensor by combining the excellent electrical properties of rGO and sensing capabilities of $CuFe_2O_4$. The nanocomposite was characterized using FTIR, Raman spectroscopy, XRD, XPS, TEM) and N_2 adsorption-desorption analysis. The designed sensor can detect NH_3 at low concentrations up to 5 ppm at room temperature. Ahmad et al. (Ahmad et al., 2018) synthesized Polyaniline@graphene/nickel oxide (Pani@GN/NiO), polyaniline/graphene (Pani/GN), and polyaniline/nickel oxide (Pani/NiO) nanocomposites. They were successfully used for ammonia sensing and were characterized using XRD, UV–vis spectroscopy, Raman spectroscopy, SEM and TEM.

Chen et al. (Chen et al., 2018) developed Graphene oxide and cuprous oxide (GO/Cu2O) nanocomposite based quartz crystal microbalance (QCM) gas sensor via layer-by-layer self-assembly (LBLSA) method for trimethylamine (TMA) gas sensing under concentrations of 5 ppm. The sensor response increased linearly with the concentration of TMA, which was consistent with the Saurebrey equation. It also had good sensitivity, reversibility, selectivity and stability in 60 days. The detection limit of 230 ppb was achieved which was the lowest detection levels among recently reported QCM gas sensor towards TMA under room temperature.

4. Conclusion

This review article investigates the GR and related nanocomposites with their industrial applications. There are many advantageous of GR, such as small volume and consequently lighter weight, resistant to temperature changes. However, there are specific disadvantageous, such as manipulation of these materials due to their small size. These materials are also expensive and lacking of comprehensive studies showing the main concepts regarding their potentials to be employed in industrial applications. GR can be categorized in two main categories: graphene oxide and rGO. Both are used in numerous applications such as biotechnology, nanoelectronics, supercapacitors and biosensors. Nanocomposite section was given in parts such as polymer/GR, metal

oxide/GR and carbon fibres/GR. In the last section, the usage of GR nanocomposite was presented in industrial applications, including supercapacitors, biosensors, solar cells, membrane, corrosion, membrane and gas sensor.

Despite progress and advances in the fabrication of graphene nanocomposite biosensors and their characterisation, there are still several challenges related to practical implementation, including limited lifetime, operational stability and reproducibility. In future, it is expected that a wide range of new graphene-based nanocomposites using different polymer hosts (thermoplastic, thermosetting, and especially commodity polymers) and a wide range of graphene nanoelements (with different functionalities, size and shape) will be published.

Declaration of interest statement

The authors declare that they have no known competing financial interests or personal relationships that could have appeared to influence the work reported in this paper.

References

Achary, L.S.K., Kumar, A., Barik, B., Nayak, P.S., Tripathy, N., Kar, J.P., Dash, P., 2018. Sensor. Actuator. B Chem. 272, 100–109.
Aghazadeh, M., 2018. Analytical and Bioanalytical Electrochemistry 10 (8), 961–973.
Ahirrao, D.J., Mohanapriya, K., Jha, N., 2018. Mater. Res. Bull. 108, 73–82.
Ahmad, S., Ali Khan, M.M., Mohammad, F., 2018. ACS Omega 3 (8), 9378–9387.
Akyüz, D., Koca, A., 2018. J. Photochem. Photobiol. A Chem. 364, 625–634.
Alomair, N.A., Mohamed, H.H., 2018. Mater. Res. Express 5 (9).
Altuntas, D.B., Tepeli, Y., Anik, U., 2016. 2D Mater. 3 (3).
Amin, S., D, M.R.G., Hamid Reza, N., 2017. Appl. Surf. Sci. 402, 245–253.
An, X., Yu, X., Yu, J.C., Zhang, G., 2013. J. Mater. Chem. 1 (16), 5158–5164.
Araque, E., Villalonga, R., Gamella, M., Martínez-Ruiz, P., Reviejo, J., Pingarrón, J.M., 2013. J. Mater. Chem. B 1 (17), 2289–2296.
Arduini, F., Cinti, S., Scognamiglio, V., Moscone, D., 2016. Microchimica Acta 183 (7), 2063–2083.
Arukula, R., Vinothkannan, M., Kim, A.R., Yoo, D.J., 2019. J. Alloy. Comp. 771, 477–488.
Ates, M., Caliskan, S., Özten, E., 2018. J. Solid State Electrochem. 22 (10), 3261–3271.
Aydın, C., 2019. J. Alloy. Comp. 771, 964–972.
Aziz, T.N.T.A., Rosli, A.B., Yusoff, M.M., Herman, S.H., Zulkifli, Z., 2019. Mater. Sci. Semicond. Process. 89, 68–76.
Bagheri, H., Afkhami, A., Khoshsafar, H., Rezaei, M., Sabounchei, S.J., Sarlakifar, M., 2015. Anal. Chim. Acta 870 (1), 56–66.
Bahadır, E.B., Sezgintürk, M.K., 2016. Trac. Trends Anal. Chem. 76, 1–14.
Bai, Z., Zhou, C., Xu, H., Wang, G., Pang, H., Ma, H., 2017. Sensor. Actuator. B Chem. 243, 361–371.
Balamurugan, J., Thanh, T.D., Kim, N.H., Lee, J.H., 2016. Biosens. Bioelectron. 83, 68–76.
Bao, C., He, Q., Han, J., Cheng, J., Zhang, R., 2018. J. Solid State Electrochem. 22 (9), 2917–2928.
Baruah, B., Kumar, A., 2018. Synth. Met. 245, 74–86.
Ben Haj Othmen, W., Hamdi, A., Addad, A., Sieber, B., Elhouichet, H., Szunerits, S., Boukherroub, R., 2018. Chemistry 367, 145–155.
Beura, R., Thangadurai, P., 2018. J. Environ. Chem. Eng. 6 (4), 5087–5100.
Borah, M.J., Devi, A., Saikia, R.A., Deka, D., 2018. Energy 158, 881–889.
Borisova, B., Sánchez, A., Jiménez-Falcao, S., Martín, M., Salazar, P., Parrado, C., Pingarrón, J.M., Villalonga, R., 2016. Sensor. Actuator. B Chem. 232, 84–90.
Botcha, V.D., Sutar, D.S., Major, S.S., 2018. J. Phys. Chem. Solids 118, 158–165.
Boujakhrout, A., Sánchez, A., Díez, P., Jiménez-Falcao, S., Martínez-Ruiz, P., Peña-Álvarez, M., Pingarrón, J.M., Villalonga, R., 2015. J. Mater. Chem. B 3 (17), 3518–3524.
Celik, N., W. Balachandran and N. Manivannan, 2015 9(6): 434-445.
Cernat, A., Tertiş, M., Săndulescu, R., Bedioui, F., Cristea, A., Cristea, C., 2015. Anal. Chim. Acta 886, 16–28.
Chauhan, N., Chawla, S., Pundir, C.S., Jain, U., 2017. Biosens. Bioelectron. 89, 377–383.
Chauhan, P.S., Kant, R., Rai, A., Gupta, A., Bhattacharya, S., 2019. Mater. Sci. Semicond. Process. 89, 6–17.
Chen, J.-L., Yan, X.-P., Meng, K., Wang, S.-F., 2011. Anal. Chem. 83 (22), 8787–8793.
Chen, L., Zheng, H., Zhu, X., Lin, Z., Guo, L., Qiu, B., Chen, G., Chen, Z.N., 2013. Analyst 138 (12), 3490–3493.
Chen, Q., Sun, T., Song, X., Ran, Q., Yu, C., Yang, J., Feng, H., Yu, L., Wei, D., 2017. Nanotechnology 28 (31).
Chen, T., Zhou, Y., Zhang, J., Cao, Y., 2018. INt. J. Electrochem. Sci. 13 (9), 8575–8588.
Cheng, Y., Sun, C., Liu, R., Yang, J., D. J, 2019. Angewandte Chemie International Edition, vol. 58. pp. 5049–5053.
Chien, H.H., Cheng, Y.C., Hao, Y.C., Hsu, C.C., Cheng, I.C., Yu, I.S., Chen, J.Z., 2018. Diam. Relat. Mater. 88, 23–31.
Chou, C.T., Wang, F.H., 2018. J. Vac. Sci. Technol. A: Vacuum, Surfaces and Films 36 (5).
Dargahi, Z., Asgharzadeh, H., Maleki-Ghaleh, H., 2018. Ceram. Int. 44 (11), 13015–13023.
Das, S., Sa, K., Alam, I., Mahanandia, P., 2018. Mater. Lett. 232, 232–236.
Davoodi, A.H., Mazinani, S., Sharif, F., Ranaei-Siadat, S.O., 2018. J. Polym. Res. 25 (9).
Dong, W.C., Hyun, J.C., Alan, F., Jong, B.B., 2014. J. Mater. Chem. 2, 12136–12149.
Du, Y., Dong, S., 2017. Anal. Chem. 89 (1), 189–215.
Du, X., Jiang, D., Chen, S., Dai, L., Zhou, L., Hao, N., You, T., Mao, H., Wang, K., 2017. Biosens. Bioelectron. 89, 681–688.
Du, H., Gui, X., Yang, R., Zhang, H., Lin, Z., Liang, B., Chen, W., Zhu, H., Chen, J., 2018. J. Mater. Sci. 53 (20), 14619–14628.
Dutta, D., Ganda, A.N.F., Chih, J.K., Huang, C.C., Tseng, C.J., Su, C.Y., 2018. Nanoscale 10 (26), 12612–12624.
Dwivedi, D., Lepková, K., Becker, T., 2017. RSC Adv. pp. 4580–4610.
Farajvand, M., Farajzadeh, K., Faghani, G., 2018. Mater. Res. Express 5 (7).
Feng, X., Cheng, H., Pan, Y., Zheng, H., 2015. Biosens. Bioelectron. 70, 411–417.
Gao, F., Yang, C.-L., Wang, M.-S., Ma, X.-G., Liu, W.-W., 2019. Spectrochim. Acta Mol. Biomol. Spectrosc. 206, 216–223.
Giuri, A., Colella, S., Listorti, A., Rizzo, A., Mele, C., Corcione, C.E., 2018. Compos. B Eng. 148, 149–155.
Gokoglan, T.C., Soylemez, S., Kesik, M., Dogru, I.B., Turel, O., Yuksel, R., Unalan, H.E., Toppare, L., 2017. Food Chem. 220, 299–305.
Guan, L.Z., Zhao, L., Wan, Y.J., Tang, L.C., 2018. Nanoscale 10 (31), 14788–14811.
Gulati, U., Chinna Rajesh, U., Rawat, D.S., 2018. ACS Sustain. Chem. Eng. 6 (8), 10039–10051.
Gupta, S., Meek, R., 2018. Sensor. Actuator. B Chem. 274, 85–101.
Gupta, A., Jamatia, R., Patil, R.A., Ma, Y.R., Pal, A.K., 2018. ACS Omega 3 (7), 7288–7299.
Hafeez, H.Y., Lakhera, S.K., Karthik, P., Anpo, M., Neppolian, B., 2018. Appl. Surf. Sci. 449, 772–779.
Hatamluyi, B., Es'haghi, Z., 2018. Electroanalysis 30 (8), 1651–1660.
Hossain, M.F., Park, J.Y., 2016. Scientific Reports 6.
Hu, X., Wang, G., Wang, B., Liu, X., Wang, H., 2019. Chem. Eng. J. 355, 986–998.
Huang, H., Bai, W., Dong, C., Guo, R., Liu, Z., 2015. Biosens. Bioelectron. 68, 442–446.
Huang, W., Ding, S., Chen, Y., Hao, W., Lai, X., Peng, J., Tu, J., Cao, Y., Li, X., 2017. Sci. Rep. 7 (1), 5220.
Huang, J., Tang, X., Li, Z., Liu, K., 2018. J. Colloid Interface Sci. 532, 407–415.
Huang, Y., Lin, L., Shi, T., Cheng, S., Zhong, Y., Chen, C., Tang, Z., 2019. Appl. Surf. Sci. 463, 498–503.
Hui, Y., Ma, X., Hou, X., Chen, F., Yu, J., 2015. Ionics 21 (6), 1751–1759.
Hummers, W.S., Offeman, R.E., 1958. J. Am. Chem. Soc. 80, 1339.
Jamil, A., Lim, H.N., Yusof, N.A., Tajudin, A.A., Huang, N.M., Pandikumar, A., Golsheikh, A.M., Lee, Y.H., Andou, Y., 2015. Sensor. Actuator. B Chem. 221, 1423–1432.
Jasmi, F., Azeman, N.H., Bakar, A.A.A., Zan, M.S.D., Badri, K.H., Su'ait, M.S., 2018. IEEE Access.
Jayachandiran, J., Yesuraj, J., Arivanandhan, M., Raja, A., Suthanthiraraj, S.A., Jayavel, R., Nedumaran, D., 2018. J. Inorg. Organomet. Polym. Mater. 28 (5), 2046–2055.
Jia, Y., Li, S., Gao, J., Zhu, G., Zhang, F., Shi, X., Huang, Y., Liu, C., 2019. Appl. Catal. B Environ. 240, 241–252.
Jiang, L., Syed, J.A., Lu, H., Meng, X., 2019. J. Alloy. Comp. 770, 35–47.
Jin, K., Zhang, W., Wang, Y., Guo, X., Chen, Z., Li, L., Zhang, Y., Wang, Z., Chen, J., Sun, L., Zhang, T., 2018. Electrochim. Acta 285, 221–229.
Jin, J.U., Lee, D.H., Nam, K.H., Yu, J., Kim, Y.K., Goh, M., Kim, S.G., Lee, H.S., Ku, B.C., You, N.H., 2019. Appl. Surf. Sci. 464, 509–515.
Jose, P.P.A., Kala, M.S., Kalarikkal, N., Thomas, S., 2018. Res. Chem. Intermed. 44 (9), 5597–5621.
Karachi, N., Hosseini, M., Parsaee, Z., Razavi, R., 2018. J. Photochem. Photobiol. A Chem. 364, 344–354.
Kausar, A., 2018. Int. J. Polym. Anal. Charact. 23 (5), 450–462.
Kim, S., Ou, R., Hu, Y., Li, X., Zhang, H., Simon, G.P., Wang, H., 2018. J. Membr. Sci. 562, 47–55.
Ko, J.S., Kim, H.S., Kosowska, K., Domalik-Pyzik, P., Nocuń, M., Chłopek, J., 2018. Mater. Chem. Phys. 216, 28–36.
Kumar, A., Prajapati, P.K., Pal, U., Jain, S.L., 2018a. ACS Sustain. Chem. Eng. 6 (7), 8201–8211.
Kumar, N., Rodriguez, J.R., Pol, V.G., Sen, A., 2019. Appl. Surf. Sci. 463, 132–140.
Kurbanoglu, S., Rivas, L., Ozkan, S.A., Merkoçi, A., 2017. Biosens. Bioelectron. 88, 122–129.
Labhane, P.K., Patle, L.B., Sonawane, G.H., Sonawane, S.H., 2018. Chem. Phys. Lett. 710, 70–77.
Li, N., Than, A., Wang, X., Xu, S., Sun, L., Duan, H., Xu, C., Chen, P., 2016. ACS Nano 10 (3), 3622–3629.
Li, M., Wang, P., Li, F., Chu, Q., Li, Y., Dong, Y., 2017. Biosens. Bioelectron. 87, 752–759.
Li, H., Su, Q., Kang, J., Feng, H., Huang, P., Feng, M., Huang, M., Du, G., 2018. Mater. Res. Bull. 108, 106–112.
Liao, C., Wu, S., 2019. Chem. Eng. J. 355, 805–814.
Lin, J., Yan, S., Liu, P., Chang, X., Yao, L., Lin, H., Lu, D., Han, S., 2018. Res. Chem. Intermed. 44 (7), 4503–4518.
Liu, Z., Guo, Y., 2018. J. Electroanal. Chem. 825, 57–64.
Liu, X., Wang, F., Aizen, R., Yehezkeli, O., Willner, I., 2013. J. Am. Chem. Soc. 135 (32), 11832–11839.
Liu, F., Xiang, G., Jiang, D., Zhang, L., Chen, X., Liu, L., Luo, F., Li, Y., Liu, C., Pu, X., 2015a. Biosens. Bioelectron. 74, 214–221.
Liu, H., Chen, X., Su, X., Duan, C., Guo, K., Zhu, Z., 2015b. J. Electrochem. Soc. 162 (12), B312–B318.
Liu, H., Duan, C., Yang, C., Shen, W., Wang, F., Zhu, Z., 2015c. Sensor. Actuator. B Chem. 218, 60–66.
Liu, Y., Han, Y., Chen, R., Zhang, H., Liu, S., Liang, F., 2016. PLoS One 11 (7).
Liu, H., Guo, K., Duan, C., Dong, X., Gao, J., 2017a. Biosens. Bioelectron. 87, 473–479.
Liu, H., Guo, K., Duan, C., Dong, X., Gao, J., 2017b. Biosens. Bioelectron. 87, 473–479.

Liu, W., Ma, Y., Sun, G., Wang, S., Deng, J., Wei, H., 2017c. Biosens. Bioelectron. 92, 305–312.
Low, W.H., Khiew, P.S., Lim, S.S., Siong, C.W., Ezeigwe, E.R., 2018. J. Alloy. Comp. 768, 995–1005.
Lu, B., Yuan, X., Ren, Y., Shi, Q., Wang, S., Dong, J., Nan, Z.D., 2018. Bioelectrochemistry 123, 103–111.
Ma, L., Wang, X., Zhang, Q., Tong, X., Zhang, Y., Li, Z., 2018. Analytical Methods 10 (31), 3845–3850.
Mahvelati-Shamsabadi, T., Goharshadi, E.K., Shafaee, M., Niazi, Z., 2018. Separ. Purif. Technol. 202, 326–334.
Maity, C.K., Hatui, G., Verma, K., Udayabhanu, G., Pathak, D.D., Nayak, G.C., 2018. Vacuum 157, 145–154.
Marinoiu, A., Raceanu, M., Carcadea, E., Varlam, M., 2018. Appl. Surf. Sci. 456, 238–245.
Mathew, G., Dey, P., Das, R., Chowdhury, S.D., Paul Das, M., Veluswamy, P., Neppolian, B., Das, J., 2018. Biosens. Bioelectron. 115, 53–60.
Mehmood, U., Ahmad, S.H.A., Khan, A.U.H., Qaiser, A.A., 2018. Sol. Energy 170, 47–55.
Mijowska, E., Onyszko, M., Urbas, K., Aleksandrzak, M., Shi, X., Moszyński, D., Penkala, K., Podolski, J., El Fray, M., 2015. Appl. Surf. Sci. 355, 587–592.
Mogha, N.K., Sahu, V., Sharma, M., Sharma, R.K., Masram, D.T., 2016. Mater. Des. 111, 312–320.
Muain, M.F., Cheo, K.H., Omar, M.N., Amir Hamzah, A.S., Lim, H.N., Salleh, A.B., Tan, W.S., Tajudin, A., 2018. Bioelectrochemistry 122, 199–205.
Mukherjee, S., Meshik, X., Choi, M., Farid, S., Datta, D., Lan, Y., Poduri, S., Sarkar, K., Baterdene, U., Huang, C.E., Wang, Y.Y., Burke, P., Dutta, M., Stroscio, M.A., 2015. IEEE Trans. NanoBioscience 14 (8), 967–972.
Muthuchamy, N., Lee, K.P., Gopalan, A.I., 2017. Biosens. Bioelectron. 89, 390–399.
Nagarani, S., Sasikala, G., Satheesh, K., Yuvaraj, M., Jayavel, R., 2018. J. Mater. Sci. Mater. Electron. 29 (14), 11738–11748.
Naresh, N., Narsimulu, D., Jena, P., Srinadhu, E.S., Satyanarayana, N., 2018. J. Mater. Sci. Mater. Electron. 29 (17), 14723–14732.
Nayak, P., Santhosh, P.N., Ramaprabhu, S., 2015. J. Nanosci. Nanotechnol. 15 (7), 4855–4862.
Ndiaye, N.M., Ngom, B.D., Sylla, N.F., Masikhwa, T.M., Madito, M.J., Momodu, D., Ntsoane, T., Manyala, N., 2018. J. Colloid Interface Sci. 532, 395–406.
Olean-Oliveira, A., Teixeira, M.F.S., 2018. Sensor. Actuator. B Chem. 271, 353–357.
Oraon, R., De Adhikari, A., Tiwari, S.K., Nayak, G.C., 2016. Dalton Trans. 45 (22), 9113–9126.
Pachauri, V., Ingebrandt, S., 2016. Essays Biochem. 60 (1), 81–90.
Park, S., Lee, K.S., Bozoklu, G., Cai, W., Nguyen, S.T., Ruoff, R.S., 2008. ACS Nano 2, 572–578.
Pathak, A.K., Kumar, V., Sharma, S., Yokozeki, T., Dhakate, S.R., 2019. J. Colloid Interface Sci. 533, 548–560.
Perveen, R., Nasar, A., Inamuddin, Asiri, A.M., Mishra, A.K., 2018. Int. J. Hydrogen Energy 43 (32), 15144–15154.
Proa-Coronado, S., Vargas-García, J.R., Manzo-Robledo, A., Mendoza-Acevedo, S., Villagómez, C.J., Mercado-Zúñiga, C., Muñoz-Aguirre, N., Villa-Vargas, L.A., Martinez-Rivas, A., 2018. Thin Solid Films 658, 54–60.
Pu, N.W., Chen, C.Y., Qiu, H.X., Liu, Y.M., Song, C.H., Lin, M.H., Ger, M.D., 2018. INt. J. Electrochem. Sci. 13 (7), 6812–6823.
Puiu, M., Bala, C., 2018. Bioelectrochemistry 120, 66–75.
Punethaa, Vinay Deep, Ranab, Sravendra, Jin Yooc, Hye, Chaurasiad, A., 2017. Prog. Polym. Sci. 67, 1–47.
Qu, S., Xiong, Y., Zhang, J., 2019. Separ. Purif. Technol. 210, 382–389.
Rahmawati, R., Suendo, V., Hidayat, R., 2018. IOP Conference Series: Materials Science and Engineering.
Raicopol, M., Vlsceanu, I., Lupulescu, I., Brezoiu, A.M., Pilan, L., 2016. UPB Scientific Bulletin, Series B: Chem. Mater. Sci 78 (2), 131–142.
Ramakrishnan, S., Pradeep, K.R., Raghul, A., Senthilkumar, R., Rangarajan, M., Kothurkar, N.K., 2015. Analytical Methods 7 (2), 779–786.
Ranjbar, S., Shahrokhian, S., 2018. Bioelectrochemistry 123, 70–76.
Saeed, A.A., Sánchez, J.L.A., O'Sullivan, C.K., Abbas, M.N., 2017. Bioelectrochemistry, vol. 118. pp. 91–99.
Salimikia, I., Heydari, R., Yazdankhah, F., 2018. J. Iran. Chem. Soc. 15 (7), 1593–1601.
Sandhya, P.K., Jose, J., Sreekala, M.S., Padmanabhan, M., Kalarikkal, N., Thomas, S., 2018. Ceram. Int. 44 (13), 15092–15098.
Sephra, P.J., Baraneedharan, P., Sivakumar, M., Thangadurai, T.D., Nehru, K., 2018. Mater. Res. Bull. 106, 103–112.
Sharma, B., Malik, P., Jain, P., 2018. Mater. Today. Commun. 16, 353–363.
Sharma, R., Mahto, V., Vuthaluru, H., 2019. Fuel 235, 1245–1259.
Shoja, Y., Kermanpur, A., Karimzadeh, F., 2018. Biosens. Bioelectron. 113, 108–115.
Siddique, S., Iqbal, M.Z., Mukhtar, H., 2017. Sensor. Actuator. B Chem. 253, 559–565.
Singu, B.S., Yoon, K.R., 2019. J. Alloy. Comp. 770, 1189–1199.
Song, W., Wang, B., Fan, L., Ge, F., Wang, C., 2019. Appl. Surf. Sci. 463, 403–411.
Sukhrobov, P., Numonov, S., Gao, S., Mamat, X., Wagberg, T., Guo, Y., Liu, L., Hu, G., 2018. Nano 13 (7).
Sun, Y., He, K., Zhang, Z., Zhou, A., Duan, H., 2015. Biosens. Bioelectron. 68, 358–364.
Sundriyal, S., Sharma, M., Kaur, A., Mishra, S., Deep, A., 2018. J. Mater. Sci. Mater. Electron. 29 (15), 12754–12764.
Suvina, V., Krishna, S.M., Nagaraju, D.H., Melo, J.S., Balakrishna, R.G., 2018. Mater. Lett. 232, 209–212.
Swain, S.S., Unnikrishnan, L., Mohanty, S., Nayak, S.K., 2018. J. Mater. Sci. 53 (22), 15442–15464.
Tabrizi, A.G., Arsalani, N., Mohammadi, A., Ghadimi, L.S., Ahadzadeh, I., 2018. J. Colloid Interface Sci. 531, 369–381.
Taheri, N.N., Ramezanzadeh, B., Mahdavian, M., Bahlakeh, G., 2018. J. Ind. Eng. Chem. 63, 322–339.
Teymourian, H., Salimi, A., Khezrian, S., 2017. Electroanalysis 29 (2), 409–414.
Tian, J., Wang, J., Li, Y., Huang, M., Lu, J., 2017. J. Electrochem. Soc. 164 (7), H470–H476.
Tian, C., Wang, L., Luan, F., Zhuang, X., 2019. Talanta, vol. 191. pp. 103–108.
Timoumi, A., Alamri, S.N., Alamri, H., 2018. Results in Physics 11, 46–51.
Ton, N.N.T., Dao, A.T.N., Kato, K., Ikenaga, T., Trinh, D.X., Taniike, T., 2018. Carbon 133, 109–117.
Veeramani, V., Dinesh, B., Chen, S.M., Saraswathi, R., 2016. J. Mater. Chem. 4 (9), 3304–3315.
Velmurugan, V., Srinivasarao, U., Ramachandran, R., Saranya, M., Grace, A.N., 2016. Marer-Res-Bullet 84, 145–151.
Wan, Y., Li, J., Yang, Z., Ao, H., Xiong, L., Luo, H., 2018. Curr. Appl. Phys. 18 (8), 933–940.
Wang, B., Akiba, U., Anzai, J.I., 2017. Molecules 22 (7), 3–8.
Wang, M., Yu, X., Hou, L., Gagnoud, A., Fautrelle, Y., Moreau, R., Li, X., 2018. Chem. Eng. J. 351, 930–938.
Wang, A.-Y., Chaudhary, M., Lin, T.-W., 2019. Chem. Eng. J. 355, 830–839.
Wu, F., Xu, F., Chen, L., Jiang, B., Sun, W., Wei, X., 2016. Chem. Res. Chin. Univ. 32 (3), 468–473.
Wu, L., Lu, X., Fu, X., Wu, L., Liu, H., 2017. Sci. Rep. 7 (1).
Wu, F., Wu, X., Duan, Z., Huang, Y., Lou, X., F, X., 2019. mall 7, 5–9.
Xi, J., Xie, C., Zhang, Y., Wang, L., Xiao, J., Duan, X., Ren, J., Xiao, F., Wang, S., 2016. ACS Appl. Mater. Interfaces 8 (34), 22563–22573.
Xiao, B., Zhang, B., Tang, L.B., An, C.S., He, Z.J., Tong, H., Yu, W.J., Zheng, J.C., 2018. Ceram. Int. 44 (13), 15044–15049.
Xie, R., Wang, Z., Zhou, W., Liu, Y., Fan, L., Li, Y., Li, X., 2016. Analytical Methods 8 (20), 4001–4006.
Xing, L.L., Wu, X., Huang, K.J., 2018. J. Colloid Interface Sci. 529, 171–179.
Xu, X., Zheng, Q., Bai, G., Song, L., Yao, Y., Cao, X., Liu, S., Yao, C., 2017. Electrochim. Acta 242, 56–65.
Xu, D., Cheng, B., Wang, W., Jiang, C., Yu, J., 2018. Appl. Catal. B Environ. 231, 368–380.
Xu, D., Xiong, X., Chen, P., Yu, Q., Chu, H., Yang, S., Wang, Q., 2019. J. Magn. Magn. Mater. 469, 428–436.
Xuan, X., Kim, J.Y., Hui, X., Das, P.S., Yoon, H.S., Park, J.Y., 2018. Biosens. Bioelectron. 120, 160–167.
Xue, Y., Huang, Y., Zhou, Z., Li, G., 2018. IOP Conference Series: Materials Science and Engineering.
Xue, X.Z., Zhang, J.Y., Zhou, D., Liu, J.K., 2019. Dyes Pigments 160, 109–118.
Yan, J., Zhong, T., Qi, W., Wang, H., 2015. J. Inorg. Organomet. Polym. Mater. 25 (2), 275–281.
Yang, M., Kim, D.S., Lee, T.J., Lee, S.J., Lee, K.G., Choi, B.G., 2016. J. Colloid Interface Sci. 468, 51–56.
Yang, Z., Hao, X., Chen, S., Ma, Z., Wang, W., Wang, C., Yue, L., Sun, H., Shao, Q., Murugadoss, V., Guo, Z., 2019. J. Colloid Interface Sci. 533, 13–23.
Yarahmadi, E., Didehban, K., Shabanian, M., Saeb, M.R., 2018. A glimpse at cure kinetics and fracture behavior. Progress in Color, Colorants and Coatings 11 (1), 55–62.
Yasin, G., Arif, M., Shakeel, M., Dun, Y., Zuo, Y., Khan, W.Q., Tang, Y., Khan, A., Nadeem, M., 2018. Adv. Eng. Mater. 20 (7).
Yu, N., Wang, Z., Wang, C., Han, J., Bu, H., 2017. Anal. Chim. Acta 962, 24–31.
Yuan, Wanga, Maoa, Pandong, Yanb, Fangfang, Gaob, Chengwei, Liub, Yanhui, Dingb, Jie, Wua, Weina, Y.L, 2016. Synth. Met. 222, 198–204 *.
Yusoff, N., Rameshkumar, P., Mehmood, M.S., Pandikumar, A., Lee, H.W., Huang, N.M., 2017. Biosens. Bioelectron. 87, 1020–1028.
Zabihi, Z., Rodriguez, P.E.D.S., Boujakhrout, A., Viera, J.C., del Valle, J.A., Araghi, H., Villalonga, R., 2018. J. Appl. Polym. Sci. 135 (37).
Zan, X., Bai, H., Wang, C., Zhao, F., Duan, H., 2016. Chem. Eur J. 22 (15), 5204–5210.
Zang, G., Hao, W., Li, X., Huang, S., Gan, J., Luo, Z., Zhang, Y., 2018. Electrochim. Acta 277, 176–184.
Zhang, M., Liao, C., Yao, Y., Liu, Z., Gong, F., Yan, F., 2014. Adv. Funct. Mater. 24 (7), 978–985.
Zhang, W., Han, C., Jia, B., Saint, C., Nadagouda, M., Falaras, P., Sygellou, L., Vogiazi, V., Dionysiou, D.D., 2017. Electrochim. Acta 236, 319–327.
Zhang, B., Li, C., Zhang, H., Chen, Y., Jiang, H., Chen, L., Ur Rehman, F., Wang, X., 2018. J. Biomed. Nanotechnol. 14 (7), 1277–1286.
Zhao, Y., Huo, D., Bao, J., Yang, M., Chen, M., Hou, J., Fa, H., Hou, C., 2017. Sensor. Actuator. B Chem. 244, 1037–1044.
Zhao, W., Liu, H., Meng, N., Jian, M., Wang, H., Zhang, X., 2018. J. Membr. Sci. 565, 380–389.
Zheng, C., Zhou, X., Cao, H., Wang, G., Liu, Z., 2014. J. Power Sources 3, 75–79.
Zheng, L., Zheng, H., Huo, D., Wu, F., Shao, L., Zheng, P., Jiang, Y., Zheng, X., Qiu, X., Liu, Y., Zhang, Y., 2018. Sci. Rep. 8 (1).
Zhou, Y., Li, J., Liu, C., Huo, P., Wang, H., 2018. Appl. Surf. Sci. 458, 586–596.
Zhou, F., Liao, N., Zhang, M., Xue, W., 2019. Appl. Surf. Sci. 463, 610–615.
Zhu, Y., Lu, S., Gowri Manohari, A., Dong, X., Chen, F., Xu, W., Shi, Z., Xu, C., 2017. J. Electroanal. Chem. 796, 75–81.